AGU PUBLICATIONS

Reviews of Geophysics

REVIEW ARTICLE

10.1002/2014RG000450

Key Points:
- Tide model accuracy assessment
- Improved accuracies
- Tidal current estimates

Correspondence to:
D. Stammer,
detlef.stammer@zmaw.de

Citation:
Stammer, D., et al. (2014), Accuracy assessment of global barotropic ocean tide models, *Rev. Geophys.*, *52*, 243–282, doi:10.1002/2014RG000450.

Received 24 FEB 2014
Accepted 13 JUL 2014
Accepted article online 18 JUL 2014
Published online 7 AUG 2014

Accuracy assessment of global barotropic ocean tide models

D. Stammer[1], R. D. Ray[2], O. B. Andersen[3], B. K. Arbic[4], W. Bosch[5], L. Carrère[6], Y. Cheng[3,7], D. S. Chinn[8], B. D. Dushaw[4], G. D. Egbert[9], S. Y. Erofeeva[9], H. S. Fok[10,11], J. A. M. Green[12], S. Griffiths[13], M. A. King[14], V. Lapin[13], F. G. Lemoine[2], S. B. Luthcke[2], F. Lyard[6], J. Morison[15], M. Müller[16], L. Padman[17], J. G. Richman[18], J. F. Shriver[18], C. K. Shum[11,19], E. Taguchi[1], and Y. Yi[11]

[1]Centrum für Erdsystemforschung und Nachhaltigkeit, Universität Hamburg, Hamburg, Germany, [2]NASA Goddard Space Flight Center, Greenbelt, Maryland, USA, [3]DTU Space, Technical University of Denmark, Copenhagen, Denmark, [4]Department of Earth and Environmental Science, University of Michigan, Ann Arbor, Michigan, USA, [5]Deutsches Geodätisches Forschungsinstitut, Munich, Germany, [6]LEGOS, UMR 5566, Observatoire Midi-Pyrénées, Toulouse, France, [7]School of Marine Sciences, Nanjing University of Information Science and Technology, Nanjing, China, [8]SGT Inc., NASA/GSFC, Greenbelt, Maryland, USA, [9]College of Earth, Ocean, and Atmospheric Sciences, Oregon State University, Corvallis, Oregon, USA, [10]Now at School of Geodesy and Geomatics, Wuhan University, Wuhan, China, [11]Division of Geodetic Science, School of Earth Sciences, Ohio State University, Columbus, Ohio, USA, [12]School of Ocean Sciences, Bangor University, Menai Bridge, UK, [13]Department of Applied Mathematics, University of Leeds, Leeds, UK, [14]Surveying and Spatial Sciences Group, School of Land and Food, University of Tasmania, Hobart, Tasmania, Australia, [15]Polar Science Center, Applied Physics Laboratory, University of Washington, Seattle, Washington, USA, [16]Norwegian Meteorological Institute, Oslo, Norway, [17]Earth and Space Research, Corvallis, Oregon, USA, [18]Oceanography Division, Naval Research Laboratory, Stennis Space Center, Hancock County, Mississippi, USA, [19]Institute of Geodesy and Geophysics, Chinese Academy of Sciences, Wuhan, China

Abstract The accuracy of state-of-the-art global barotropic tide models is assessed using bottom pressure data, coastal tide gauges, satellite altimetry, various geodetic data on Antarctic ice shelves, and independent tracked satellite orbit perturbations. Tide models under review include empirical, purely hydrodynamic ("forward"), and assimilative dynamical, i.e., constrained by observations. Ten dominant tidal constituents in the diurnal, semidiurnal, and quarter-diurnal bands are considered. Since the last major model comparison project in 1997, models have improved markedly, especially in shallow-water regions and also in the deep ocean. The root-sum-square differences between tide observations and the best models for eight major constituents are approximately 0.9, 5.0, and 6.5 cm for pelagic, shelf, and coastal conditions, respectively. Large intermodel discrepancies occur in high latitudes, but testing in those regions is impeded by the paucity of high-quality in situ tide records. Long-wavelength components of models tested by analyzing satellite laser ranging measurements suggest that several models are comparably accurate for use in precise orbit determination, but analyses of GRACE intersatellite ranging data show that all models are still imperfect on basin and subbasin scales, especially near Antarctica. For the M_2 constituent, errors in purely hydrodynamic models are now almost comparable to the 1980-era Schwiderski empirical solution, indicating marked advancement in dynamical modeling. Assessing model accuracy using tidal currents remains problematic owing to uncertainties in in situ current meter estimates and the inability to isolate the barotropic mode. Velocity tests against both acoustic tomography and current meters do confirm that assimilative models perform better than purely hydrodynamic models.

1. Introduction

Tidal signals permeate the entire Earth system. An accurate knowledge of tides is consequently needed for an astonishing variety of geophysical fields ranging from the orbit of the moon to the mixing of the oceans, from solid-earth geophysics to coastal flooding [e.g., *Lambeck*, 1988; *Munk*, 1997; *Wilhelm et al.*, 1997; *Vlasenko et al.*, 2005]. An especially important application for accurate tide models is providing tide "corrections" to various measurements so that smaller nontidal signals may be studied. For example, barotropic tide models are used regularly to remove tidal variability from space geodetic observations; this is a critical necessity for successful satellite altimetry [e.g., *Fu and Cazenave*, 2001] and satellite gravimetry [*Seeber*, 2003; *Visser et al.*, 2010], and in both cases improved tidal corrections lead to a reduction of aliased tidal "noise" in nontidal signals of interest.

Much progress has been achieved in recent years in improving global tide models. In no small part, this progress has been both motivated by and the result of satellite altimetry. For more than two decades altimetry has been providing critical information needed to constrain models. Yet substantial progress is still required to reduce errors in presently used models. For example, errors in basin-scale tide prediction are roughly comparable to measurement errors of present-day satellite gravimetry and they exceed expected errors of future gravimeters by an order of magnitude or more [*Koop and Rummel*, 2008; *Wiese*, 2011; *Wiese et al.*, 2011]. Other model inadequacies will become evident in the discussions below.

Since the pioneering works of *Pekeris and Accad* [1969], *Schwiderski* [1979], and *Parke and Hendershott* [1980], several generations of tide models have passed, each leading to further improvements. The last truly comprehensive assessment of global ocean tide models was published by *Shum et al.* [1997, henceforth Shum97] only a few years after the launch of the Topex/Poseidon (T/P) satellite, a mission whose orbit was specifically designed to measure tides — which it did with remarkable success. Shum97 documented the degree of improvement of global tide models that resulted from the analysis and assimilation of only a few years of T/P data, aiming in particular to identify the next model to be included in the altimetric Geophysical Data Record (GDR) processing. For that purpose they used a variety of tests based on comparisons to in situ data, including tide gauges and bottom pressure recorders, as well as superconducting gravimeters and satellite measurements.

During the 17 years since Shum97 was published, the field has advanced considerably. We have witnessed not only improved global tidal atlases but also a much deeper insight into the dynamics of global tides. Our understanding of energy dissipation, the role of baroclinic processes in the energy budget, and the subsequent fate of tidal energy and its wider implications have all seen marked progress, and these topics continue to be at the forefront of modern research.

The central goal of this paper is to update the review of Shum97 and document the considerable advances in global barotropic tidal models themselves. All global models analyzed here were submitted by developers willing to have their work subjected to extensive tests and comparisons. The main focus of the paper lies in the sea level representation of the main tidal constituents in modern tide models, including M_2, S_2, N_2, K_2, O_1, P_1, Q_1, K_1, M_4, and MS_4 (see standard texts, e.g., *Pugh* [1987] and *Pugh and Woodworth* [2014], for the periods, relative amplitudes, and astronomical origins of these constituents). The primary models being tested are all barotropic models tightly constrained by satellite altimeter data, and these models are all found to be very accurate, even by standards of only a few years ago. We employ many of the same tests performed by Shum97, but extensive improvements have been made to some of the test data. For example, the expanded tsunami warning network [*Bernard et al.*, 2010] has provided new seafloor pressure measurements in regions previously lacking in situ data. New data sets are now available over polar seas, including valuable new tidal GPS measurements obtained on floating ice shelves [*King et al.*, 2011a, 2011b] as well as new satellites capable of providing critical polar observations, such as the ICESat and CryoSat-2 altimeter missions and the Gravity Recovery and Climate Experiment (GRACE) gravimeter mission.

With these new test data sets in hand, we took the opportunity to test several recent purely hydrodynamic numerical tide models (hereafter also referred to as "forward," "unconstrained," and "non-data-assimilating" models), which are unconstrained by any tidal observations. Comparisons of the unconstrained hydrodynamic models are limited to the M_2 component. Finally, we attempt an assessment of the accuracy of barotropic tidal currents, although not all models include estimates for currents. This assessment builds on earlier efforts by *Luyten and Stommel* [1991], *Dushaw et al.* [1997], and *Ray* [2001] but is limited mostly to the M_2 constituent. The sections on forward models and tidal currents include results from two recent models which simultaneously simulate tides and the oceanic general circulation; although such models include internal (baroclinic) tides, the evaluations of such models here are confined to barotropic elevations and currents, consistent with the emphasis of this paper.

One important subject not addressed here is the long-period tides, which are forced by the zonal potential with periods from 1 week to 18.6 years [*Wunsch*, 1967]. In general, these constituents are smaller than the short-period constituents considered in this paper, and fewer models have been developed and released. The main reason for the omission of long-period tides, however, is the lack of high-quality test data sets of harmonic constants comparable to those available for short-period tides. In particular, in the deep ocean, the most reliable test data set is probably still that developed by D. Luther, based on the analysis of 24 Pacific island tide gauges [*Miller et al.*, 1993]. There is great need for a more comprehensive global test data set for

Table 1. Participating Ocean Tide Models

Model	Type[a]	Resolution	Authors
Modern data-constrained models			
GOT4.8	E	1/2 °	*Ray* [1999, updated]
OSU12	E	1/4 °	*Fok* [2012]
DTU10	E	1/8 °	*Cheng and Andersen* [2011]
EOT11a	E	1/8 °	*Savcenko and Bosch* [2012]
HAM12	H	1/8 °	*Taguchi et al.* [2014]
FES12	H	1/16 °	*Lyard et al.* [2006, updated]
TPXO8	H	1/30 °	*Egbert and Erofeeva* [2002, updated]
Historical models			
NSWC	H	1°	*Schwiderski* [1979]
CSR3.0	E	1°	*Eanes and Bettadpur* [1996]
Purely hydrodynamic models			
HIM	N	1/8 °	*Arbic et al.* [2008]
OTIS-GN	N	1/8 °	*Green and Nycander* [2013]
STORMTIDE	N	1/10 °	*Müller et al.* [2012]
OTIS-ERB	N	1/12 °	*Egbert et al.* [2004]
STM-1B	N	1/12 °	*Hill et al.* [2011]
HYCOM	N	1/12.5 °	*Arbic et al.* [2010, updated]

[a]E, empirical adjustment to an adopted prior model; H, assimilation into a barotropic hydrodynamic model; N, purely hydrodynamic (no data constraints).

long-period tides, but this requires very long time series to extract these small signals from the red-noise background variability.

The remainder of the paper is structured as follows: in section 2 we briefly summarize all models involved in the quality assessment. Section 3 provides a summary assessment of differences between data-constrained (empirical and hydrodynamic) tide models. Section 4 evaluates the models against in situ data, separately for the nonpolar deep ocean and for shelf regions. Except for a few stations involving one model, these in situ data are independent of all tested models. Section 5 focuses on an evaluation of tide models in high latitudes based on tide gauge, bottom pressure, and GPS data. Section 6 is concerned with testing the tide models against various kinds of satellite data, including satellite gravity data, which are completely independent of all models, and satellite altimeter data, some independent of the models and some not. Section 7 is concerned with purely hydrodynamic models and their ability to simulate observed tidal heights. Section 8 then tests barotropic tidal currents from data-constrained and forward models against estimates available from moored current meters and from acoustic tomography. A summary and an outlook are provided in section 9.

2. Summary of Participating Tide Models

The following subsections give a brief overview of the tide models evaluated in this study. We structure the discussion into (i) seven modern (hydrodynamic and empirical) tide models involving data (assimilation), (ii) two historical tide models, and (iii) six hydrodynamic forward models simulating tides by imposing the respective forcing without any data constraints.

2.1. Modern Tide Models

Modern tidal models can be classified as (1) empirical adjustment to an adopted prior model and (2) barotropic hydrodynamic models constrained by tide information through assimilation. The participating seven models are listed in the upper part of Table 1. As can be seen from the table, nominal model resolutions vary from 7.5′ to 30′. The first four models described below are semiempirical ("semi" because some of their small-scale features can arise from their underlying prior models), while the last three are barotropic hydrodynamical models constrained by assimilation. All assimilative models include the constituents M_2, S_2, N_2, K_2, O_1, P_1, Q_1, and K_1. In addition, some also provide M_4, MS_4, and possibly other compound tides.

2.1.1. GOT4.8

The GOT4.8 model was developed at Goddard Space Flight Center and follows a long series of similar efforts starting with *Schrama and Ray* [1994] and *Ray* [1999]. Like several of the other models, it is the result of an empirical harmonic analysis of satellite altimetry relative to an adopted prior model. In this case the prior

was a collection of both global and regional models blended at mutual boundaries. Of the modern models examined here GOT4.8 has the coarsest spatial resolution of 0.5°, and it is therefore expected to be less accurate in near-coastal water.

In the deep ocean between latitudes ±66 °, the GOT4.8 solution was based only on data from the T/P satellite, including its extended mission along an interlaced ground track; no Jason data were used, in part to facilitate some consistency checks between T/P and Jason [*Ray*, 2013, Appendix A]. In shallow seas and also in deep water poleward of 66°, data from Geosat Follow-On, ERS-1, and ERS-2 were used. A small amount of early ICESat data were used in the Weddell and Ross seas. The load tide, i.e., the Earth's crustal deformation under the weight of the overlying ocean tide, was accounted for by an iterative method [*Cartwright and Ray*, 1991]. Note that the earlier version GOT4.7 is identical to GOT4.8 except for the S_2 constituent. The later version accounts for a small error caused by the S_2 atmospheric tide in the T/P dry-troposphere correction. Correcting for this small error makes a noticeable improvement in the final S_2 ocean tide solution [*Ray*, 2013].

Barotropic currents were derived from the GOT4.8 elevations through a least squares solution of the two-dimensional momentum and continuity equations [*Ray*, 2001].

2.1.2. OSU12

OSU12 is a global ocean tide model developed at the Ohio State University (OSU) [*Fok*, 2012]. It is an empirical ocean tide model determined using an extended orthogonal representation of the response method [*Groves and Reynolds*, 1975]. A spatiotemporal weighting algorithm was employed for the solution to combine multimission radar altimeter data with distinct tidal aliasing characteristics, spatial and temporal coverage, and accuracy. These data included T/P, Jason-1, Geosat Follow-On (GFO), and Envisat, covering the period October 1992 through January 2009, with latitude coverage limited within ±66° and load tide corrections based on the NAO99.b model of *Matsumoto et al.* [2000]. Outside the ±66° latitude bounds, the current OSU12v1.0 model is patched using the values from the GOT4.7 model; however, efforts are underway to extend the OSU12 tide model to cover the polar oceans. The OSU12 model is released with eight major semidiurnal and diurnal tides, together with the S_1 and M_4 tides. The model is available at http://geodeticscience.org/oceantides/OSU12v1.0, where future updates to the model will also be hosted.

2.1.3. DTU10

The DTU10 global ocean tide model [*Cheng and Andersen*, 2011] is based on an empirical correction to the global tide model FES2004 [*Lyard et al.*, 2006], in which the largest residual tides were determined using the response method. In order to improve shallow-water tides, 4 years of the Topex/Jason-1 interleaved mission data were introduced. Combined Envisat, GEOSAT Follow-On, and ERS-2 data sets were introduced outside the ±66° parallels to derive tides in the polar seas. As Envisat and ERS-2 were Sun-synchronous satellites, diurnal tides could be significantly improved by removing annual sea level variations prior to estimating the residual tides. The four major semidiurnal and diurnal tides were interpolated onto a regular 0.125° by 0.125° grid using a depth-dependent interpolation method [*Andersen*, 1995, 1999]. The load model used is that of FES2004. The model can be downloaded via ftp://ftp.space.dtu.dk/pub/DTU10/.

2.1.4. EOT11a

EOT11a [*Savcenko and Bosch*, 2012] is the latest version of a series of global ocean tide models, derived at Deutsches Geodätisches Forschungsinstitut (DGFI) by means of empirical analysis of multimission satellite altimetry data. EOT11 is used for reprocessing of GRACE gravity data [*Bosch et al.*, 2009]; it is based on sea surface heights observed by Topex, Jason-1, Jason-2, ERS-2, and Envisat over the ice-free oceans covering altogether the period October 1992 to March 2010. Tidal constituents were estimated based on a residual least squares harmonic analysis with FES2004 taken as reference model. EOT11a is provided on the same regular 1/8 ° grid as FES2004. At latitudes poleward of ±81.5 ° (the latitude limits of ERS-2 and Envisat) EOT11a defaults back to FES2004. The EOT11a methodology accounted for correlations among the along-track altimeter observations, applied a careful editing procedure, and used a variance component estimate in order to achieve a relative weighting of data from different missions. In addition, EOT11a solved for mission-specific offsets to account for residual altimeter biases. An analysis of the variance-covariance matrix indicated only small correlations among all constituents commonly estimated. Therefore, EOT11a is composed of individual constituents taken from different solutions with varying smoothing scales, with preference given to those solutions leading to minimal root-mean-square (RMS) differences to validation data. The load tides were computed following the algorithm of *Cartwright and Ray* [1991]. Model fields can

be downloaded at ftp://ftp.dgfi.badw.de/pub/EOT11a/data and are described in detail by *Savcenko and Bosch* [2012].

2.1.5. HAMTIDE

The HAMTIDE12 (HAM12, for short) model is a global ocean barotropic data-assimilative model developed at the University of Hamburg [*Zahel*, 1995; *Taguchi et al.*, 2014]. The model is based on the linearized tidal hydrodynamic equations and on a simple harmonic time dependence of the variables. The model includes the full loading and self-attraction (LSA) effect (also known as SAL [*Hendershott*, 1972]). Finite difference methods were adopted for numerically solving the equations. The continuous space-time domain was converted into the FES2004 [*Lyard et al.*, 2006] discrete grid domain, where the grid spacing becomes smaller in higher latitudes. The bottom topography is based on the GEBCO 1′ bathymetry field. EOT11a output was used between 74°N and 84°S as a constraint. A direct optimization method was used for finding the minimum of a cost function containing dynamical residual smoothing terms, which are the first and the second derivatives of the model residuals. Thus, the model does not smooth control variables directly. The adopted numerical assimilation scheme allows some compensation for model deficiencies [*Taguchi et al.*, 2014].

2.1.6. FES2012

FES2012 (FES12, for short) is the most recent of a series of global finite element tidal solutions, initiated by *Le Provost et al.* [1994]. The FES12 atlas [*Carrère et al.*, 2012] is built upon altimetry-derived harmonic constant assimilation using the ensemble, frequency domain SpEnOI (Spectral Ensemble Optimal Interpolation) data assimilation software in T-UGOm (Toulouse-Unstructured Grid Ocean model) hydrodynamic tidal solutions. T-UGOm is a 2-D/3-D ocean hydrodynamics model based on unstructured meshes. It has been carried out in time-stepping mode and frequency domain mode. Frequency domain 2-D governing equations are derived from the classical shallow-water continuity and momentum equations, as described in *Lyard et al.* [2006]. The horizontal discretization used for FES12 is continuous Lagrange polynomial second-order interpolation (LGP2) for elevation and discontinuous nonconforming P1 (linear approximation with nodes located at element side midpoints) for tidal currents. Resolution varies from a few kilometers in coastal areas up to about 25 km in the deep ocean. The unstructured grid covers the global ocean, with the required topography based on a number of sources, including approximately 20 regional terrain models, with considerable effort devoted to improving shelf and ice-shelf seas. Ensembles were built by perturbing the main tidal parameters, e.g., bathymetry, bottom friction, and internal tide drag. The density of data used in assimilation was tuned as a function of depth. In addition to T/P, Jason-1, and Jason-2 data which are the FES12 main assimilation data sources, interleaved mission data have been added in some regions showing small-scale tidal patterns. Similarly, ERS-1, ERS-2, and Envisat data have been used in the Arctic. GLORYS2-V1 (Global Ocean Reanalysis 2 Version 1) reanalysis [*Ferry et al.*, 2012] was used to remove nontidal annual and semiannual contributions from altimetry harmonic analysis, and GOT4.8 was used for load tide corrections.

2.1.7. TPXO8

TPXO8 is the most recent in a series of tidal solutions (elevations plus barotropic currents) produced using the representer-based variational scheme described by *Egbert et al.* [1994] and *Egbert and Erofeeva* [2002] to assimilate altimetry (and other) data into a global shallow-water model. The TPXO8-atlas solution discussed in this paper represents a further refinement, with a series of over 30 regional assimilation solutions incorporated to increase resolution in coastal areas and shallow seas. The base global solution has a resolution of 1/6°, with bathymetry for the dynamical model derived from the GEBCO 1′ database [*GEBCO Digital Atlas*, 2003] with some adjustments around Antarctica south of 57°S. Primary data were harmonically analyzed along-track tidal constants from 685 T/P and Jason cycles (up to 2011), with load tide corrections based on the earlier assimilation solution TPXO6.2. In the deep ocean, harmonic constants approximately every 12 km along track were assimilated. For shallower depths harmonic constants for every along-track point were used, along with data from 114 cycles of T/P on its interleaved ground track. At high latitudes, tide gauge data were also assimilated, including 83 around Antarctica [*King and Padman*, 2005] and 289 in the Arctic [*Kowalik and Proshutinsky*, 1994; G. Kivman, personal communication, 2002]. For the nonlinear quarter-diurnal constituents, the two-stage scheme of *Egbert et al.* [2010] was used. Regional solutions were obtained with a resolution of 1/30° for 33 rectangular areas, including all major enclosed or semienclosed seas and most coastal areas with significant continental shelf width. Higher-resolution local bathymetry was used wherever possible, and all available T/P-Jason and interleaved data were assimilated. At high latitudes, or in shallow areas with sparse T/P coverage, ERS/Envisat data were also used for lunar tides. Additional coastal tide gauges were used in some regional solutions to improve estimates in local bays (see http://volkov.oce.orst.edu/tides/region.html). The regional solutions were patched into the global

TPXO8 base solution, keeping higher resolution in coastal/shallow areas and using a weighted average of regional and global solutions over a narrow strip for a smooth transition to the global model in the open ocean. TPXO8-atlas is available in a multiresolution version, but the fixed 2′ grid was used in all tests performed here.

2.2. Historical Tide Models

To help gauge the progress that has occurred over the years, we give statistics for two historical models in a few sections below. We use one model from the era before T/P and one which was developed shortly after the launch of T/P and which was recommended by Shum97. Respective models are listed in the middle part of Table 1.

2.2.1. NSWC

The most widely adopted global tidal model in the pre-T/P era was developed at the U.S. Naval Surface Weapons Center (NSWC) by *Schwiderski* [1979]. He employed a large database of coastal and island harmonic constants and assimilated them into a 1° barotropic tidal model using a method he called "hydrodynamic interpolation," which seems to have been a variation of what is now understood as a relaxation or "nudging" method of assimilation [*Egbert and Bennett*, 1996]. Where he had good data to guide the model, his results were quite good. However, in some wide expanses of the open ocean, such as the mid-Atlantic, errors in excess of 10 cm were later found [e.g., *Cartwright and Ray*, 1990].

2.2.2. CSR3.0

One of the objectives of Shum97 was to select a tidal model for subsequent reprocessing of satellite altimeter data. Based on various rankings, they recommended the CSR3.0 model, developed by *Eanes and Bettadpur* [1996]. Those authors had used a response analysis applied to 2.4 years of T/P data. They adopted a prior hydrodynamic model based primarily on FES94 of *Le Provost et al.* [1994]. The adjustment to FES94 was heavily smoothed, which worked well over the open ocean but was probably less suitable for regions near land, a point that becomes clear in some of our tests below (e.g., see section 4). But in the deep open ocean, which has been the primary domain of satellite altimetry, CSR3.0 represented the new paradigm of tidal accuracy made possible by T/P.

2.3. Purely Hydrodynamic Models

Besides data-constrained models, purely hydrodynamic (forward) tide models are also tested in this paper with respect to their skill in simulating the M_2 barotropic tidal currents and sea surface elevations. All respective models are listed in the lower part of Table 1. The first four of the participating forward models described below are barotropic, while the latter two are baroclinic ocean general circulation models with concurrent atmospheric and tidal forcing.

2.3.1. HIM

The barotropic version of the Hallberg Isopycnal Model (HIM) [*Hallberg and Rhines*, 1996] has been utilized in a number of tidal studies, beginning with *Arbic et al.* [2004]. The simulations were run on a latitude-longitude grid from 86°S to 82°N, with an artificial wall at the northern boundary. The source topography files are described in detail in *Arbic et al.* [2004]; in brief, the topography equatorward of 72° is taken from *Smith and Sandwell* [1997], with specialized Arctic and Antarctic topographic data sets blended in at higher latitudes. Similar to other recent forward tide models [e.g., *Jayne and St. Laurent*, 2001], the HIM simulations employ a parameterized topographic wave drag to represent the tidal energy loss occurring in regions of strong internal wave generation over rough topography [*Egbert and Ray*, 2000]. As in *Egbert et al.* [2004], the HIM simulations utilize an iterative method to compute the SAL term. The particular simulation used here is the 1/8° simulation of *Arbic et al.* [2008], which yields more accurate tides than the coarser resolution runs of *Arbic et al.* [2004].

2.3.2. OTIS-ERB

The OTIS-ERB solution was derived by time-stepping the nonlinear shallow-water equations, with forcing at the M_2 and K_1 frequencies, on a 1/12° finite difference grid running from 86°S to 82°N. The numerical discretization and much of the software are identical to that used for the data-assimilating solution TPXO8. Dissipation was parameterized as a sum of a quadratic term, representing bottom friction in shallow seas, and a linear internal wave drag, comparable to that used by *Jayne and St. Laurent* [2001]. SAL was rigorously modeled with an iterative scheme, first suggested by *Accad and Pekeris* [1978]; these second-order forcing terms were computed by high-degree spherical harmonic series. Further details on the implementation and validation of the OTIS-ERB solution are provided in *Egbert et al.* [2004].

2.3.3. OTIS-GN

The OTIS-GN model presented by *Green and Nycander* [2013] is basically the same model as OTIS-ERB [*Egbert et al.*, 2004] with a resolution of 1/8° but with a few additional modifications. Firstly, the domain for OTIS-GN spans 80°S to 80°N, with elevations from TPXO.6.2 being used as boundary conditions. The second major change was that a modified tidal conversion parameterization based on the scheme presented by *Nycander* [2005] was used. The original parameterization was modified to describe the tidal conversion in terms of a 2×2 tensor rather than a two-dimensional vector (see *Green and Nycander* [2013] for further details).

2.3.4. STM-1B

STM-1B is a depth-averaged hydrodynamic tidal model, formulated in terms of the barotropic shallow-water equations in volume transport form. A spectral approach is used, in which the equations of motion are projected onto a set of discrete tidal frequencies, so that the time dependence is removed, leaving a set of partial differential equations in latitude and longitude. Nonlinearity in the momentum equation is neglected, apart from the parameterized bottom drag term, which takes the standard form $\rho c_d |\mathbf{u}|\mathbf{u}$. An iterative scheme is required to account for the parameterized nonlinear bottom drag and to allow for a full implementation of the SAL term using spherical harmonic transforms (which correspond to a dense matrix operation). A frequency-dependent linear internal tide drag parameterization is used [*Griffiths and Peltier*, 2009]. The model uses a rotated pole (passing through Greenland and Antarctica) and is thus truly global. Further details of this iterative numerical scheme are given by *Hill et al.* [2011]. Model results were calculated with a grid spacing of 1/12° (2160×4320 grid points), with forcing from three semidiurnal constituents (M_2, S_2, and N_2) and two diurnal constituents (K_1 and O_1). In the ocean interior, energy-conserving second-order finite differencing is used on an Arakawa C grid. However, the coastal boundary conditions were implemented using a standard C grid staircase coastal methodology, which degrades the overall accuracy of the solution to first order in grid spacing [*Griffiths*, 2013].

2.3.5. STORMTIDE

The STORMTIDE model [*Müller et al.*, 2012] is a high-resolution ocean circulation and tide model which resolves mesoscale eddies and low-mode internal tides. It has been developed in the framework of the German consortium project STORM, which aims for a climate model simulation at the highest resolution currently possible [*von Storch et al.*, 2012]. The ocean model includes an embedded thermodynamic sea ice model and is based on the Max-Planck Institute Ocean Model [*Marsland et al.*, 2003] but formulated on a tripolar grid. Ocean tides are forced in real time by a lunisolar tidal potential of second degree, described by analytical ephemerides. Further, the model is forced by a climatological wind forcing, which includes changes on a daily basis with a 365 day cycle. Sea surface temperature and salinity values are restored to monthly climatological values, in order to simulate a realistic seasonal cycle of mixed layer depths. The grid of the model has 40 vertical z levels and a horizontal resolution of about 0.1°. The SAL effect is considered in parameterized form. The model includes no internal wave drag; instead, in the deep ocean the four largest tidal constituents (M_2, S_2, K_1, and O_1) convert 1.1 TW of tidal energy from barotropic to baroclinic tides [*Müller*, 2013]. The model topography is based on the bathymetry SRTM30_plus (v6) [*Becker et al.*, 2009].

2.3.6. HYCOM

This baroclinic tide model employs the forward (nonassimilative) simulations of the HYbrid Coordinate Ocean Model (HYCOM), run at high vertical and horizontal resolution and forced by the astronomical tidal potential as well as by wind and buoyancy forcing. *Chassignet et al.* [2007], *Metzger et al.* [2010], and references therein provide detailed descriptions of HYCOM, while *Arbic et al.* [2010, 2012], respectively, provide details and an overview of the implementation of tides in HYCOM. The HYCOM simulations used here have 32 layers in the vertical direction and an equatorial horizontal resolution of 1/12.5°. The land-sea boundary is set at the 10 m isobath. The bottom topography is derived from the Naval Research Laboratory Digital Bathymetry Data Base (DBDB2), which has a resolution of 2 min and is available online at http://www7320.nrlssc.navy.mil/DBDB2_WWW/. Numerous hand edits were performed to improve coastlines and sill depths in key straits and passages. The model utilizes a "tripolar" grid and is therefore truly global. The SAL effect is currently treated with the simplified scalar approximation of *Accad and Pekeris* [1978]. As in the forward barotropic studies described earlier, a parameterized topographic wave drag is employed in the HYCOM simulations to account for the breaking of unresolved high vertical mode internal waves (see *Arbic et al.* [2010] for more discussion). The simulations were run interannually over the period July 2003 to December 2010 using 6-hourly Fleet Numerical Oceanography Center Navy Operational Global Atmospheric Prediction System [*Rosmond et al.*, 2002] atmospheric forcing with wind speeds scaled to be consistent with QuikSCAT [e.g., *Liu and Xie*, 2006] observations. The HYCOM surface tidal elevations used here were taken from *Shriver*

Table 2. Standard Deviations of Differences Between Tidal Models and Their RSS[a]

Water Depth	Q_1	O_1	P_1	K_1	N_2	M_2	S_2	K_2	RSS
Global	0.22	0.60	0.32	1.02	0.50	1.84	0.86	0.34	2.458
> 1000 m	0.15	0.23	0.14	0.30	0.22	0.30	0.24	0.19	0.646
< 1000 m	0.23	0.66	0.38	1.12	0.78	3.39	1.50	0.50	4.061

[a]Only data-constrained models listed in Table 1 are included in this comparison. RSS, root-sum-square.

et al. [2012] and are based on an analysis of year 2006. For the barotropic tidal current analysis in section 8, just 1 month of model output (September 2004, output at hourly intervals) was used owing to the enormous amount of storage needed for a high-resolution three-dimensional global model.

3. Elevation Differences Between Modern Tide Models

Following *Andersen et al.* [1995], the standard deviation (SD) of the seven tide models listed in the top part of Table 1 was computed with respect to elevations $\eta_j = \zeta_j e^{-i\sigma t}$, where ζ_j is a time-independent amplitude of a tide (e.g., M_2 tide) at a wet grid point j, σ denotes its frequency, and $i = \sqrt{-1}$. As a first step of the computation, the mean elevation of each tidal constituent across all models ($N = 7$) was computed at every grid point according to

$$\eta_{\text{mean}} = \frac{1}{N}\sum_{j=1}^{N} \zeta_j e^{-i\sigma t} = H_{\text{mean}} \left(\cos G_{\text{mean}} + i \sin G_{\text{mean}}\right) e^{-i\sigma t}. \tag{1}$$

Here $\zeta_j = H_j \left(\cos G_j + i \sin G_j\right)$ with amplitude H_j and Greenwich phase lag G_j (hereafter, "Greenwich" is dropped and the term "phase lag" is understood to be in reference to Greenwich, as is standard in tidal studies). The SD between all involved models can then be computed for each constituent according to

$$\begin{aligned} \text{SD}_{\text{tide}} &= \left(\frac{1}{N}\sum_{n=1}^{N} \frac{1}{T}\int_0^T \left(Re(\eta_n - \eta_{\text{mean}})\right)^2 \text{d}t \right)^{1/2} \\ &= \left(\frac{1}{N}\sum_{n=1}^{N} \frac{1}{2}\left[\left(H_n \cos(G_n) - H_{\text{mean}} \cos(G_{\text{mean}})\right)^2 + \left(H_n \sin(G_n) - H_{\text{mean}} \sin(G_{\text{mean}})\right)^2 \right] \right)^{1/2}, \end{aligned} \tag{2}$$

where H_n and G_n are the amplitude and Greenwich phase lag of a constituent given by each model, respectively, and H_{mean} and G_{mean} are the amplitude and Greenwich phase lag for the averages of equation (1). The SD of all present models for the tide (M_2, for example) is computed according to

$$\text{SD}_{\text{tide}} = \left(\frac{1}{P}\sum_{k=1}^{P} (\text{SD}_{\text{tide}}^k \cos(\phi_k))^2 \right)^{1/2}. \tag{3}$$

Here k is the grid point index, P is the number of all elevation grid (wet) points, and ϕ_k is the latitude of grid point k.

Computations of SD_{tide} were performed for the tidal constituents M_2, S_2, N_2, K_2, K_1, O_1, P_1, and Q_1 after regridding bilinearly the fields of every model to a common 0.5° grid. Results are summarized in Table 2 for the global ocean and separately for the deep ocean (> 1000 m depth) and the shallow seas (< 1000 m depth), respectively. As an example, the SD of all models is 1.87 cm for M_2 which is 13% lower than the 2.29 cm obtained by Shum97. In the case of K_1, the SD of 1.02 cm exceeds the value of 0.89 cm obtained by Shum97, suggesting that the present models diverge more from each other than was the case previously. However, Shum97 did not include polar regions and was significantly less inclusive in shallow seas, both areas where quite large SD values (often > 2 cm for both M_2 and K_1 tides) occur. Moreover, present models agree much better with each other over the deep ocean (SD = 0.3 cm) as compared to Shum97, who reported a SD of 0.5–1.0 cm for both M_2 and K_1 tides in the deep sea (> 1000 m).

Spatial patterns of the SD of model differences are displayed in Figures 1 (top) and 1 (bottom) for M_2 and K_1, respectively. Clearly, the SD of both constituents is large in polar regions, especially in the Ross and Weddell Seas in the Antarctic and in Baffin Bay, between Greenland and Ellesmere Island. The same holds

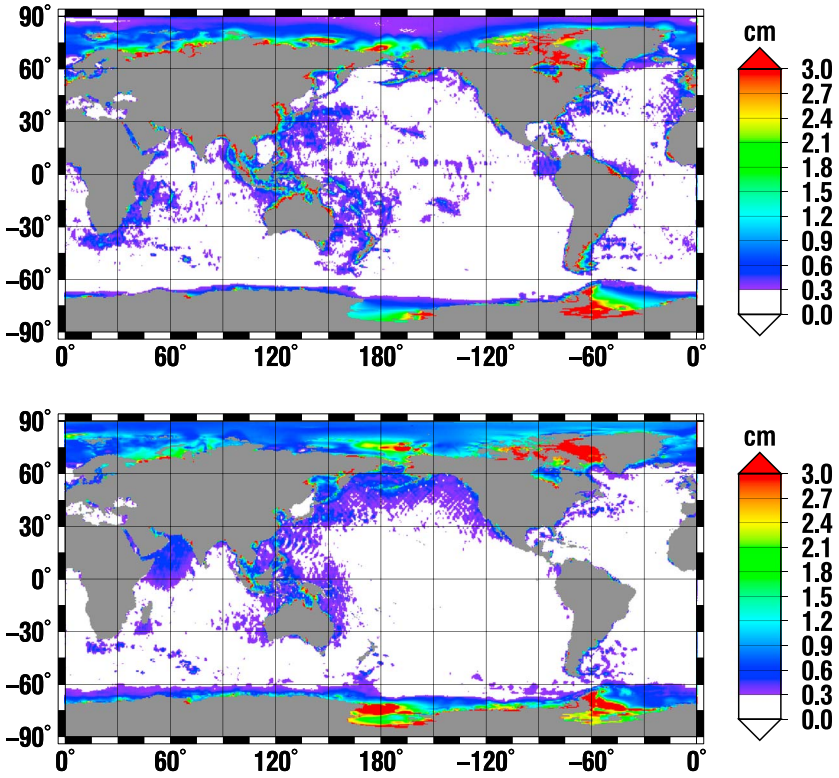

Figure 1. Standard deviations for (top) M_2 and (bottom) K_1 from the seven modern data-constrained models listed in Table 1.

for the other tidal constituents (not shown) and presumably results from the lack of observations there. However, we note that the largest discrepancies between models can be found in the coastal Arctic regions for which most of the tide gauge information is available, not in the center of the Arctic where tidal amplitudes are much smaller (see also section 5.1). In the Antarctic the largest model discrepancies are located under the ice shelves; an exception is K_1 for which the largest errors are in the open continental shelf areas of the western Ross and western Weddell Seas. The SD of semidiurnal tides are also enhanced in the western portions of the Pacific and Indian Oceans, characterized by complex topography and in some cases also extreme tidal amplitudes (e.g., along the northern Australian continent, in the Mozambique Channel, and in the Atlantic on the Patagonian Shelf), along the northeastern coast of Brazil and along the track of the Gulf Stream, where the magnitude of the SD is between 0.3 and 1.2 cm for M_2 and S_2 tides and 0.3 and 0.6 cm for N_2 and K_2 tides. Large SD of diurnal tides resides in the most northern part of the Pacific Ocean with magnitudes of 0.3 to 1.2 cm for K_1 and O_1 tides and 0.3 to 0.6 cm for P_1 and Q_1 tides. Large SD is also found in the western parts of the Pacific Ocean and in the Arabian Sea. In the Atlantic Ocean, SD for diurnal tides is small everywhere owing to the generally small amplitudes of diurnal tides. Enhanced model discrepancies in eddy-rich western boundary current regions presumably point toward eddy energy aliased into tide models there. We also note that intermodel discrepancies appear to be substantially elevated in shelf regions relative to the open ocean where an overall RSS value over the eight constituents is less than 1 cm.

4. Tests of Modern Tide Models Against Tide Gauge Data

Comparisons with in situ "ground truth" tidal measurements form one of the most straightforward, yet powerful, tests of model output. The test data used here are considerably improved and extended over those used by Shum97. Three primary data sets are used, one based in deep water, one in shelf water and shallow seas, and one along coastlines of continents. (Polar regions are reserved for section 5.) The philosophy for separating the tests in this way rests with the different role that satellite altimetry plays in each regime. Deep-ocean tides, for example, are determined primarily by direct constraints from satellite altimeter measurements, especially from Topex/Poseidon and the Jason follow-on missions. Similarly, shelf tides can also be determined in large part by altimetry, especially multimission altimetry [e.g., *Cheng and Andersen*,

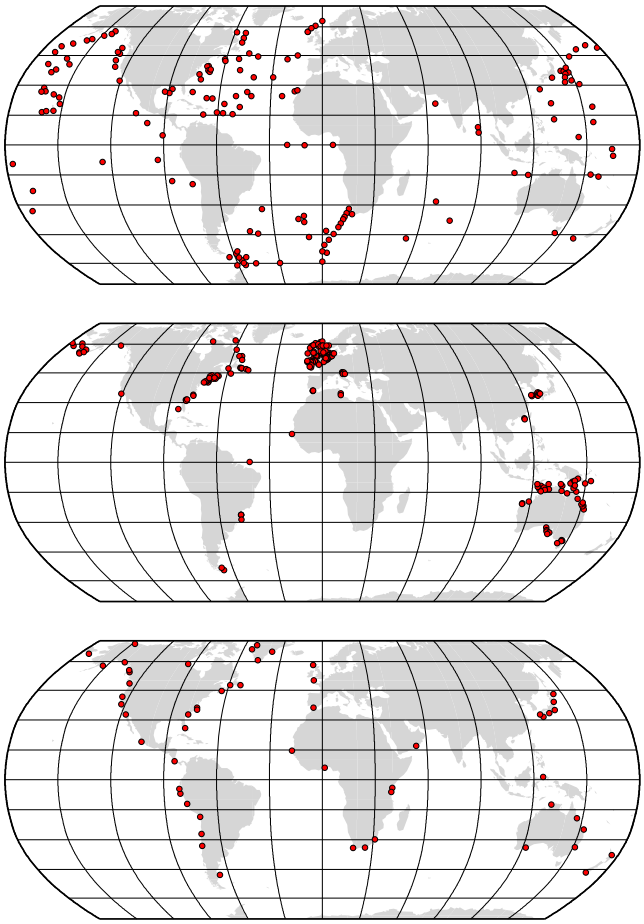

Figure 2. Station locations for the "ground truth" tidal data used in section 4. (top) Deep-water stations. (middle) Shelf stations. (bottom) Coastal stations.

2011], although the determination is more difficult because of the shorter scale of shelf tides, necessitating hydrodynamic assimilation (or the use of hydrodynamic priors for empirical models). For truly coastal tides, however, altimetry plays little role except as distant constraints, and accuracies generally must rely on hydrodynamic modeling and an accurate bathymetry [e.g., *Ray et al.*, 2011].

The following comparisons test individual tidal constituents, focusing on major constituents that are released by all or most models under study. At each comparison station, tidal constants from the models are interpolated to the station location by bilinear interpolation. Station locations are shown in Figure 2, separated into (top) deep, (middle) shelf, and (bottom) coastal stations.

Testing individual tidal constituents does have one important limitation. Many users of tidal models require only accurate height predictions, and they are less concerned with individual constituents. Errors in a few major constituents do not give a complete accounting of errors in height prediction. This is probably not a great concern for deep water, since forming an RSS across the eight major constituents should yield a rough guide to prediction error. In shallow water, however, where dozens (or more) compound tides may be required for accurate prediction, our reliance on a few constituents—and indeed the tested models' similar reliance on the same—is inadequate. These matters are discussed further by *Ray et al.* [2011], who attempt to gauge the errors of omission in tidal prediction. For present purposes the main implication is that our statistics in sections 4.2 and 4.3 must be considered optimistic as a guide to overall tidal height prediction. In some shallow-water regions it is possible that the omission error from missing constituents is comparable to, or exceeds, the error in the M_2 constituent, which normally dominates the error spectrum.

4.1. Deep-Ocean Gauges

The deep-ocean test data consist of harmonic constants at 151 sites, all deduced from long time series of pressure measurements taken on the seafloor (Figure 2, top). All are independent of the models being tested. Use of open-ocean bottom pressure avoids local tide effects that sometimes can occur even at small islands, so the data are thus comparable to the tidal fields measured by satellite. Compilation of these data is described by *Ray* [2013], who provides details regarding station selection criteria, analysis methods, and various corrections. Preference was given to long time series; the median length was 567 days. The solar semidiurnal S_2 tide in bottom pressure was corrected for the presence of the atmospheric barometric tide, using a climatological model based on operational surface pressures from the European Centre for Medium-Range Weather Forecasts (ECMWF). Conversion of bottom pressure amplitudes to equivalent sea surface heights was based on a climatological ocean density at each station location.

For all 151 stations the signals and RMS differences for major constituents are summarized in Table 3, where the first two models listed are the two historical ones dating from before and shortly after the launch

Table 3. Tide Signal and RMS Model Differences (cm) Against Deep-Ocean Bottom Pressure Recorder (BPR) Stations[a]

	Q_1	O_1	P_1	K_1	N_2	M_2	S_2	K_2	RSS	M_4
Signal	1.8	8.8	4.0	12.5	6.4	30.2	11.2	3.1		0.2
Pre-Topex/Poseidon										
NSWC	0.290	0.874	0.638	1.292	1.153	4.268	1.779	0.660	5.106	
Early Topex										
CSR3.0	0.230	0.502	0.252	0.585	0.375	0.923	0.607	0.470	1.514	
Modern models										
GOT4.8	**0.165**	0.296	0.234	0.423	0.252	**0.510**	0.369	0.209	**0.923**	0.089
OSU12	0.304	0.369	0.194	0.430	0.441	0.578	0.940	0.287	1.394	0.137
DTU10	0.226	**0.277**	0.292	0.449	0.274	0.613	0.415	0.383	1.088	0.089
EOT11a	0.232	0.317	0.224	0.404	0.335	0.564	0.428	0.365	1.056	0.282
HAM12	**0.160**	0.317	0.199	**0.373**	0.245	**0.513**	0.397	0.176	**0.904**	
FES12	0.216	0.309	0.355	0.471	0.342	0.658	0.407	0.223	1.120	0.115
TPXO8	**0.153**	0.310	**0.181**	0.442	**0.201**	**0.523**	**0.338**	**0.151**	**0.893**	**0.069**
Bootstrap σ	0.013	0.018	0.012	0.018	0.018	0.034	0.024	0.018		0.008

[a]Models listed in order of increasing spatial resolution. Bold font marks models within 1σ of the lowest RMS in any given constituent, where σ is taken from the median bootstrap of all models except NSWC, CSR, and TPXO8.

of T/P in 1992. The signal is defined by $\sqrt{\overline{A^2_{\text{station}}}/2}$, where the A_{station} values are the amplitudes at the respective stations and the overbar represents an average over all stations. The RMS difference is given by $(\overline{[A_{\text{station}}\cos(\omega t-\phi_{\text{station}})-A_{\text{model}}\cos(\omega t-\phi_{\text{model}})]^2})^{1/2}$, where here the overbar is computed over one full cycle of the constituent in question (e.g., ωt varying from 0 to 2π) as well as over all the station locations, ω is frequency, t is time, ϕ denotes phase lag, and the "model" subscript denotes model values. A striking feature of the table is the very low RMS for all modern models: half a centimeter or better for all constituents, representing relative errors (a ratio of RMS difference to signal) ranging from about 2% for M_2 up to 10% for the smaller K_2, P_1, and Q_1 constituents. In contrast, the comparable deep-ocean data set used by Shum97—a 102-station set compiled primarily by Christian Le Provost and David Cartwright—showed much larger RMS differences, e.g., 1.6 cm for M_2. We note, however, that much of the improvement here comes from the improved test data set, not improvements in the models. For example, for GOT4.8 the old 102-station test set gives an RMS of 1.45 cm [*Ray*, 2013] versus the 0.51 cm RMS value here. The new data set benefits from many newer multiyear bottom pressure time series now available, including those of the international tsunami warning network, while the old data set had many very short (30 days) bottom pressure series and some island data that were evidently biased by local harbor or lagoon perturbations. Nonetheless, Table 3 also shows good improvement over the historical models, with the RMS for CSR3.0 M_2 nearly double that of the modern models, and NSWC almost an order of magnitude worse. Most of the other constituents also show good improvement over the 1997-era "best" model.

The final line of Table 3 is our attempt to gauge statistical uncertainty in the computed RMS values in order to assess the significance of very small differences among models. For six of the models we computed a bootstrap estimate of the standard deviation of the RMS values (resampling with replacement), and the quoted entries in the table are the median standard deviations for each constituent. We consider any models having RMS values within an interval less than this bootstrap σ to be equivalent, and bold font in the table marks all models within 1σ of the lowest RMS in any given constituent.

Four of the modern models in Table 3 have at least one bold entry, indicating a best ranking in that constituent. TXPO.8 has the most such entries, with best results in all four semidiurnal constituents; only its K_1 shows somewhat higher RMS in comparison. The S_2 constituent for OSU12 is anomalous with RMS of 0.94 cm. In this case we speculate a problem with an altimeter correction, since many of these, including atmospheric delay corrections and atmospheric loading corrections, can have significant power at the S_2 frequency. An overweighting of Sun-synchronous altimeter data, which can corrupt S_2 estimates, is another potential explanation for the anomalous OSU12 S_2 RMS value.

An RMS difference is only one measure of discrepancy. To test the robustness of these results, we have also computed the median absolute difference between in-phase and quadrature components of models and test stations. Such median differences should be less sensitive to a few bad comparisons, although there are

very few of those in the deep-ocean stations. The median results are not shown here, but they are broadly consistent with results of Table 3. In particular, DTU10 shows the best ranking in O_1 and HAM12 by far the best in K_1, while TPXO8 is again best in all four semidiurnal constituents as well as in Q_1 and P_1 (with ties if statistical variability is allowed for).

4.2. Shallow/Shelf Sea Gauges

The test data of this section consist of harmonic constants from 195 stations located in water generally shallower than 200 m but not along continental coastlines (Figure 2, middle). These stations therefore represent primarily shelf tides. Given generally larger tidal amplitudes and shorter wavelengths in these regions relative to tides in the deep ocean, we must anticipate larger discrepancies with the in situ data and, as seen in section 3, among the models themselves. Nonetheless, shelf tides can be constrained by altimetric data, even if spatial resolution is challenging, and extending satellite altimetry into shallow-water regions is a topic of growing interest [e.g., *Vignudelli et al.*, 2011]. We therefore wished to design a test appropriate to shallow, but not coastal, water. Thus, in this section we avoid tide gauges located along coastlines of large land masses, although we do employ gauges at small offshore islands; this is especially the case for our data near the Australian continent, which are all offshore island gauges. Otherwise, the great majority of stations are from bottom pressure shelf measurements.

The tide gauge data here build on the data set compiled and used by *Ray et al.* [2011] but now augmented to a total of 195 stations. Newly added stations are extracted from recent publications, such as two new stations on the Patagonian Shelf off Tierra del Fuego [*Richter et al.*, 2012], or from previously overlooked publications, such as data from the Gulf of Gabes [*Sammari et al.*, 2006] and South China Sea [*Beardsley et al.*, 2004], as well as from unpublished data (e.g., data from the Savu Sea provided by Dr. Janet Sprintall, October 2009). Nevertheless, the spatial coverage of the data is still far from adequate, as is evident from Figure 2 (middle).

These shelf data are themselves much less accurate than the deep-ocean data of the previous section—they include shorter time series, stations less well documented, and stations displaying considerably higher differences with models but not obviously identifiable as being in error. In a few isolated cases we have used anomalous discrepancies with our seven primary models to identify and sometimes correct problem stations. One case involved new bottom pressure data from the northern Adriatic Sea [*Book et al.*, 2009]; corrected harmonic constants were kindly provided by Dr. Jeffrey Book. Another case involved one of the few stations from the interior of the Yellow Sea, with tidal constants published by *Teague et al.* [1998]; their Station C is located in the middle of the Yellow Sea and should be well observed by satellite, but the reported phase lag for M_2 of 169.3° is in poor agreement with our models (with values 182.7°, 182.0°, 181.8°, 183.7°, 181.8°, 182.3°, and 182.2°). The cause of this problem has not been resolved, but ultimately we removed this station from our test set. (It is worth noting that *Yao et al.* [2012], in their regional modeling of the Yellow Sea tides, obtained a phase of 181° in their unconstrained prior solution but 172° after assimilating the Station C data; we surmise that their prior may have been the more accurate at that location.) There are a few similar cases. In all cases we had confidence that any rejected tide gauge station was in a location that should have been well observed by altimetry, and yet models differed unusually from gauge estimates; otherwise we kept the gauge even if differences were large.

Of the 195 test stations, 76 are on the northwest European Shelf. To avoid overweighting that geographic region in our global statistics, and to compare consistency of statistics, Table 4 gives RMS gauge model differences split between the European Shelf and the remainder of the globe. (Unlike Table 3, Table 4 could not include the NSWC model because that model was undefined for the Mediterranean Sea and the Strait of Korea; but leaving out those stations, its RMS for M_2 is 33.1 cm, far larger than any entry in the table.) Of the 195 stations, 10 of them were assimilated by TPXO.8, mostly in the region around Australia. None of the European tide gauges were assimilated, so the assimilation affects only the lower portion of Table 4. None of the other models assimilated any of our test stations.

Unlike the deep-ocean case, now all seven modern models have at least one constituent marked as best in Table 4. As before, TPXO.8 has the most such entries, which may partly reflect its assimilation of 10 of the stations, although its performance is also excellent on the European Shelf where it assimilated no stations. For M_2 on the European Shelf, the models cluster into two groups with RMS values either less than 4 cm or greater than 5 cm. The best models are DTU10, HAM12, FES12, and TPXO8. Elsewhere, the best M_2 is DTU10,

Table 4. Tide Signal and RMS Model Differences (cm) Against Shelf Water Tide Stations[a]

	Q_1	O_1	P_1	K_1	N_2	M_2	S_2	K_2	RSS	M_4	MS4
					European Shelf						
Signal	2.1	5.6	1.5	5.5	17.0	87.7	30.0	7.3		4.7	2.9
CSR3.0	1.07	2.10	0.54	1.67	5.09	13.34	5.61	2.38	15.78		
GOT4.8	0.93	0.92	0.55	1.30	1.97	5.87	2.51	1.09	7.04	2.80	
OSU12	1.11	1.24	0.69	1.53	1.77	5.04	4.04	1.29	7.22	2.10	
DTU10	**0.83**	0.81	**0.51**	1.27	2.17	**3.50**	2.38	0.92	**5.17**	2.74	
EOT11a	**0.85**	0.83	**0.50**	**1.24**	2.13	5.53	3.43	1.13	7.17	3.16	
HAM12	0.92	1.96	**0.47**	**1.14**	1.65	**3.11**	2.64	0.92	**5.14**		
FES12	**0.88**	0.82	0.71	**1.19**	**1.39**	**3.71**	**1.94**	**0.63**	**4.82**	2.22	1.86
TPXO8	**0.88**	**0.72**	**0.46**	**1.21**	**1.58**	3.85	**1.70**	**0.74**	**4.87**	**0.35**	**1.16**
Bootstrap σ	0.05	0.08	0.07	0.11	0.20	0.70	0.46	0.14		0.35	
					Elsewhere						
Signal	2.7	11.0	6.0	17.3	12.5	53.6	21.9	7.1		1.9	1.5
CSR3.0	1.20	2.44	1.45	4.96	6.00	23.11	7.86	2.65	25.91		
GOT4.8	**0.69**	**1.05**	0.92	1.68	1.97	4.14	2.93	1.59	6.11	1.25	
OSU12	1.00	1.17	0.84	1.75	1.87	4.61	3.00	**1.15**	6.42	1.44	
DTU10	0.82	**1.11**	1.06	1.70	1.80	**3.44**	2.39	1.57	5.40	1.26	
EOT11a	**0.73**	**1.07**	**0.78**	1.64	1.86	5.05	3.39	1.31	6.87	1.11	
HAM12	0.97	1.16	**0.80**	2.02	2.01	**3.89**	2.52	1.44	5.88		
FES12	0.80	1.00	0.89	**1.51**	**1.58**	**3.33**	2.30	**1.02**	**4.96**	**0.98**	**1.33**
TPXO8[b]	0.82	**1.00**	**0.82**	**1.47**	2.00	**3.50**	**1.93**	**1.12**	**5.07**	**0.88**	1.51
Bootstrap σ	0.08	0.12	0.08	0.14	0.17	0.41	0.21	0.18		0.12	0.14

[a]Models listed in order of increasing spatial resolution. Bold font marks models within 1σ of the lowest RMS in any given constituent, where σ is taken from the median bootstrap of all models except CSR and TPXO8.

[b]TPXO8 assimilated a subset of the test stations.

FES12, HAM12, and TPXO. GOT4.8 is the poorest on the European Shelf, evidently marred by its coarse 0.5° resolution, although its statistics for "Elsewhere" are relatively good, including the best Q_1.

In shallow seas it is unclear whether the RMS statistic provides a meaningful general description of a model. This is borne out by Figure 3 which shows histograms of M_2 vector differences (absolute magnitudes) between each of the 195 stations and two models—one of the best (DTU10) according to Table 4 and one of the worst (GOT4.8). For both models, most station-model differences are small, less than 2.5 cm, but there are a number of much larger differences that will tend to skew, rightly or wrongly, an RMS statistic. The interpretation is that in most shallow-water locations the model errors in M_2 will be less than 2.5 cm, but there are still some locations (not always evident in Figure 1) where errors are much greater (tens of centimeters). As noted above the error can also be assessed by the median absolute differences in in-phase and quadrature components. Such median difference results for M_2 (not shown) vary between 1.1 cm and 1.5 cm, with DTU10 and FES12 slightly superior. We emphasize that in shallow regions one single statistic cannot adequately capture the error characteristics of these models, and a model user could well be disappointed by any of these models if the location of interest is one of the outlier stations shown in Figure 3.

4.3. Coastal Tide Gauges

Although some very high-resolution global models may yield adequate tide predictions along some coastlines, they cannot be expected to be competitive with well-constructed local models based on high-quality local bathymetric data and local tidal knowledge. Nonetheless, some assessment of the models here under consideration may be of value to those wishing to rely on global models. For example, relying on global tide models is not uncommon when corrections are needed for satellite altimetry, since local models are often unavailable while the global models are readily at hand. This section is provided primarily to stress to such users that tide model errors can be potentially very large in the near-coastal zone.

The set of coastal tide gauges used in this section is a subset of those analyzed by *Ponchaut et al.* [2001]. Those authors produced high-quality tidal analyses for gauges associated with the World Ocean Circulation Experiment, and we here adopt only those stations situated along continental coastlines (or nearby islands, such as the station at Zanzibar, Tanzania). After removing open-ocean islands from the *Ponchaut et al.* data set there are 56 stations left (Figure 2, bottom). Although this number is small compared with the total

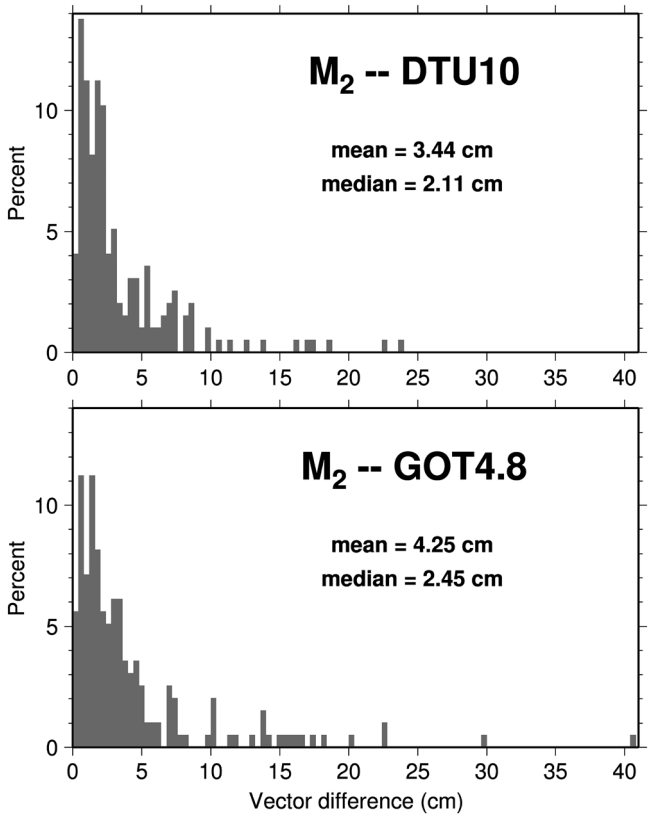

Figure 3. Histograms of M_2 vector differences (absolute magnitudes) between 195 shelf tide stations and one of the more accurate shelf tide models (DTU10) and one of the less accurate (GOT4.8) according to the statistics of Table 4. Both models evidently are reasonably accurate for most stations, with median vector differences less than 2.5 cm. However, both also show large model-gauge differences for a handful of stations. Thus, most tested models are reasonably accurate on the shelves and in shallow seas, but large errors occur in a few locations, which are not always predictable and which may surprise unwary users.

potential data set of coastal stations, the data set offers advantages of being well documented, with reliable tidal harmonic constants. For nearly all tested models, some station locations were deemed by the model to be land and a small amount of extrapolation was necessary to arrive at a valid model amplitude and phase. Of the 56 stations, two of them (both on the Australian coast) were assimilated by TPXO.8.

Table 5 shows both RMS and median absolute differences between the models and the 56 coastal stations. In this case, even more so than with the shelf tides, the RMS statistic is probably not a good general descriptor, since one or two poor stations can dominate the results. That is clearly the case for the M_2 differences of HAM12 and TPXO8, which are both anomalously large. TPXO8 has poor agreement at two difficult stations, Zanzibar and Darwin (Australia), while HAM12 is poor at Zanzibar and Ketchikan (Alaska). Another station which has poor agreement with most models is Duck (North Carolina), which sits on a barrier island that is not adequately demarcated in some models, resulting in errors, sometimes on both sides of the island—see Figure 4. While these problem stations skew the global RMS statistics, they are nonetheless instructive for the types of error that may be encountered along some coastlines.

The more robust median differences of Table 5 are much smaller than the RMS differences, indicating reasonably accurate model values for the majority of stations, with M_2 component differences between 1.0 and 1.5 cm for all seven modern models and HAM12 the best for M_2 notwithstanding its anomalous RMS. Model EOT11a may be the slightly preferred model for these 56 test sites, since both its median differences and its RMS differences are generally very good across most constituents. However, FES12 has the most bold entries for the RMS differences, and TPXO8 appears best for median differences for all constituents except for M_2.

5. High-Latitude Tides

Regions poleward of the Topex/Poseidon and Jason maximum latitude of 66°, and where sea ice and ice shelves interfere with satellite altimeter detection of the ocean surface, have lower densities of high-quality satellite and in situ data for validation and assimilation. These regions also, typically, have poor bathymetric grids, especially for regions under the large Antarctic ice shelves. In this section we report separately on tide model accuracy for the Arctic and Antarctic regions and briefly describe future prospects for improvement.

5.1. Arctic Ocean

Tide models were tested in the Arctic Ocean (latitudes >65°N) using a data set of harmonic constants for M_2, S_2, K_1, and O_1, determined previously from 240 tide gauges, with the number of stations being different for the different constituents. (The data set, developed by Z. Kowalik and A. Proshutinsky, is available at http://www.ims.uaf.edu/tide). Due to harsh conditions, Arctic tide gauges are often placed in sheltered,

Table 5. Tide Signal and RMS Model Differences (cm) With 56 Coastal Tide Gauges[a]

	Q_1	O_1	P_1	K_1	N_2	M_2	S_2	K_2	RSS	M_4
Signal	2.0	10.5	5.3	17.1	12.6	60.5	11.2	6.2		1.9
Root-Mean-Square Differences										
CSR3.0	0.70	2.77	1.46	5.03	4.62	20.74	7.84	2.31	23.53	
GOT4.8	0.46	**1.01**	**0.57**	**1.80**	**1.92**	7.00	3.53	1.34	8.46	1.23
OSU12	1.14	1.68	1.20	3.20	2.15	9.01	5.31	1.41	11.48	**0.99**
DTU10	0.62	1.29	0.73	2.08	**1.72**	**5.24**	**2.68**	1.40	**6.82**	1.23
EOT11a	0.54	1.32	0.85	2.38	**1.78**	**4.50**	**2.84**	1.49	**6.49**	**1.04**
HAM12	**0.29**	1.42	0.71	2.65	2.27	14.63	5.41	1.80	16.16	
FES12	**0.32**	**0.89**	**0.61**	**1.65**	**1.74**	6.60	**2.27**	**0.77**	7.50	1.49
TPXO8	0.43	1.13	0.93	**2.01**	3.34	15.65	7.79	2.12	18.10	1.68
Bootstrap σ	0.10	0.23	0.10	0.36	0.29	0.95	0.69	0.32		0.18
Median Absolute Differences										
CSR3.0	0.25	0.56	0.32	0.94	0.63	2.48	1.31	0.57	3.15	
GOT4.8	**0.14**	0.42	**0.27**	**0.62**	0.60	1.30	0.80	0.37	1.86	0.21
OSU12	0.35	0.46	**0.26**	**0.62**	0.59	**1.19**	1.58	0.34	2.27	0.23
DTU10	0.21	0.37	0.37	**0.67**	0.42	1.28	0.77	0.42	1.83	0.20
EOT11a	0.18	0.36	0.30	**0.61**	0.41	**1.06**	0.65	0.32	**1.56**	0.25
HAM12	**0.12**	0.46	**0.27**	0.68	0.40	**1.02**	0.66	0.28	**1.57**	
FES12	0.18	0.43	0.44	**0.66**	0.47	1.36	0.66	**0.24**	1.85	0.21
TPXO8	**0.13**	**0.26**	**0.25**	**0.58**	**0.28**	1.49	**0.49**	**0.21**	**1.75**	**0.14**
Bootstrap σ	0.02	0.05	0.03	0.09	0.06	0.23	0.11	0.04		0.03

[a]Models listed in order of increasing spatial resolution. Bold font marks models within 1σ of the smallest RMS, for a particular constituent.

narrow fjords, thus lowering the chance that these locations lie within model domains. For the investigation it was required that at least one valid model point was available close to the tide gauge position in order to interpolate the model results and to keep the tide gauge data, and because of this step many tide gauges had to be dropped from further analyses. Because the original number of tide gauges for which individual constituents are available differed, the final number of stations used in the comparison between constituents differs as well.

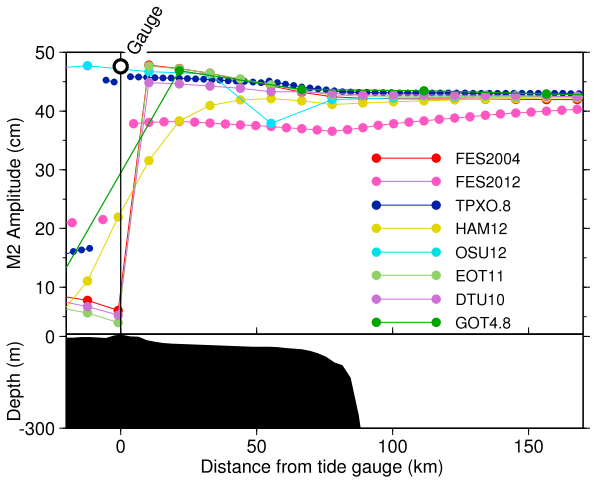

Figure 4. Amplitude of the M_2 tide near Duck Pier, North Carolina, which sits on a barrier island with the Atlantic Ocean on the east (right) and Albemarle Sound on the west (left). The tide gauge amplitude is 47.6 cm and marked by the large open circle. The gauge accurately measures the Atlantic tide; the tide in the sound is much smaller. Colored lines display model amplitudes east and west of the tide gauge, with colored dots at the resolution of each model (e.g., GOT4.8 plotted every 0.5°); unconnected dots imply that one or more model values are missing (i.e., are categorized as land). Most models are confused by the presence of the barrier island and disagree sharply in Albemarle Sound. Models DTU10 and EOT11a closely follow their prior, FES2004.

Another source of error is a seasonal variation of polar tides inferred by the seasonally varying ice coverage. In Arctic regions this effect causes changes in tidal amplitudes of *O* (1–10 cm). Since the modern tide models represent an annual mean state but most of the observation do not account for the observed seasonality, this implies some inconsistency in this model-observation evaluation.

Because the Arctic tide gauge data set has not undergone extensive quality control, we edited the data prior to the model evaluation. This was performed on the reduced 60 tide gauge set common to the five models HAM12, FES12, EOT11a, DTU10, and TPXO8; in cases where more than three models showed RSS differences for the four largest constituents greater than 15 cm with respect to the gauge data, the station was removed from the analysis.

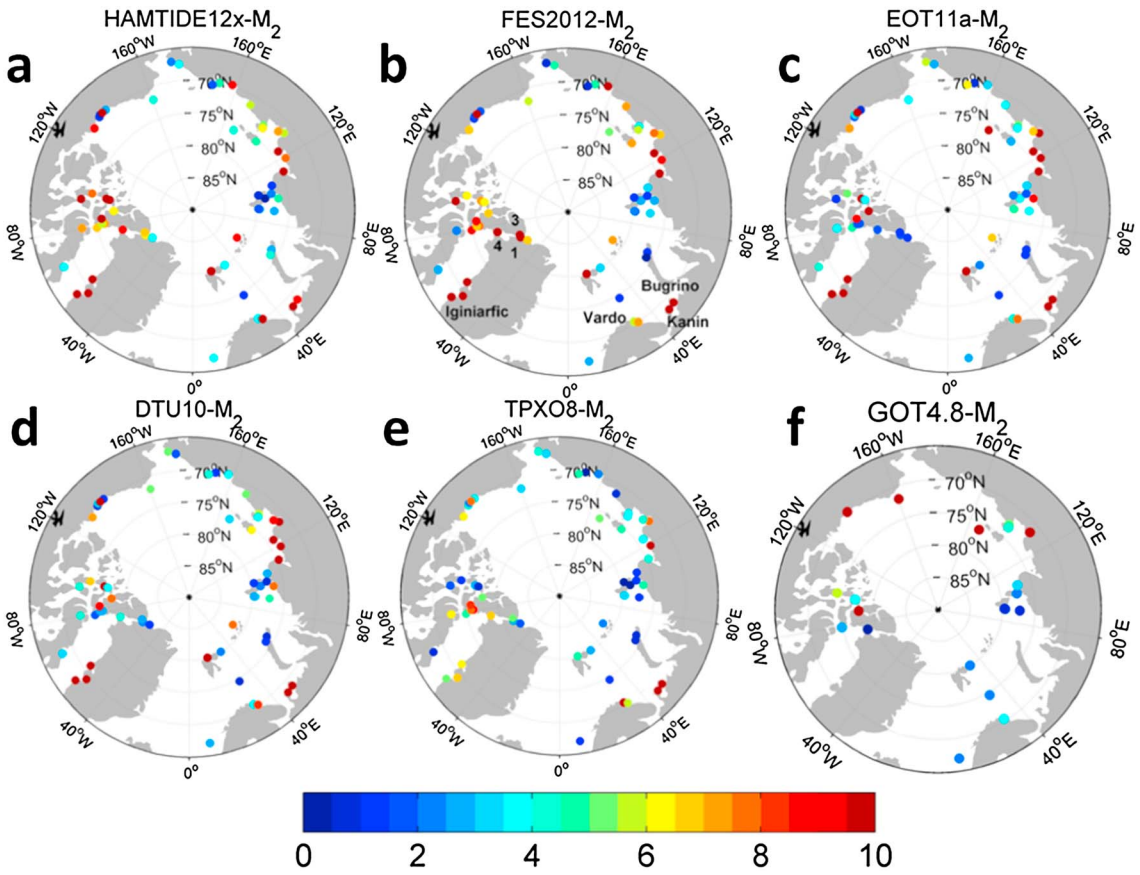

Figure 5. Magnitudes of vector differences (in cm) between in situ and bilinearly interpolated M_2 tide amplitude for 60 tide gauges for (a) HAM12, (b) FES12, (c) EOT11a, (d) DTU10, and (e) TPXO8 over the Arctic. Only 20 gauges could be used for the interpolation for (f) GOT4.8. OSU12 is identical to GOT4.8 and is therefore not shown.

This test eliminated the gauges Kanin and Bugrino (both Russia) and Iginiarfic (West Greenland). Figure 5 shows the resulting final vector differences between in situ and predicted M_2 elevation amplitude for the common tide gauges. Due to a restrictive model domain for the GOT4.8 model, only 20 gauges were used for the comparison for this model; and, as OSU12 defaults to GOT4.8 at high latitude, only the results for GOT4.8 are shown (Figure 5f). Figure 5e illustrates that TPXO8 generally has very small differences with the tide gauges, a consequence of several of these being assimilated into the model. However, a few gauge positions show enhanced differences in the southern part of the Barents Sea, e.g., Vardo (Norway), which has a very large difference for this model only, pointing toward a problem with the gauges being assimilated into the model in this region. In addition, HAM12 and FES12 both show poor agreement with three gauges in Nares Strait at the northern end of Baffin Bay. (Locations are shown by numbers 1, 3, and 4 in Figure 5b.)

The RMS and RSS for the four main tide constituents over the Arctic are shown in Table 6 for the reduced set of gauges common to all seven models. As can be seen from the table, DTU10 shows the best overall agreement with tide gauge data with an RSS of 5.7 cm, whereas all other models have RSS values in the range of 6–8 cm. It should also be noted that all gauges are coastal gauges and consequently the numbers should be compared with previous comparisons with coastal gauges for lower latitudes (see section 4.3).

For the four models not assimilating the tide gauge information (HAM12, FES12, EOT11a, and DTU10), the mean RMS difference amounts to 16% of the M_2 average amplitude and more than 30% for S_2, K_1, and O_1. This illustrates the problem that altimetric tidal models face in the Arctic. Only Sun-synchronous satellites (ERS-1, ERS-2, and Envisat), for which the S_2 is phase locked and aliases into a constant, have been available in the Arctic. Similarly, K_1 and P_1 are aliased into the annual signal.

Tide models were also tested against three bottom pressure time series in the Arctic close to the geographic North Pole: ABPR1 at 89.2543°N, 60.3597°E; ABPR3 at 89.2475°N, 148.1257°E; and ABPR4 at 89.9767°N,

Table 6. RMS and RSS Differences (Both in cm) Between the Interpolated Tidal Signal and Common Tide Gauges for the Four Major Arctic Ocean Tidal Constituents[a]

	O_1	K_1	M_2	S_2	
No. of Stations	13	16	20	15	
Signal	4.81	10.35	30.46	11.45	RSS
GOT4.8	1.78	3.20	4.83	2.24	6.47
OSU12	1.77	3.17	4.82	2.22	6.43
DTU10	1.60	2.89	3.91	2.56	5.72
EOT11a	1.36	2.85	4.61	2.44	6.09
HAM12	1.25	3.00	4.11	7.11	8.83
FES12	1.52	3.30	4.66	3.36	6.80
TPXO8[b]	1.19	1.44	5.89	1.93	6.47

[a]The average amplitude (in cm) for each tidal constituents of the Arctic is listed. The values are given for the largest common set of tide gauges to five of the models.

[b]TPXO8 model assimilates a subset of the selected in situ measurements.

178.23°E. For each bottom pressure gauge, more than 1 year of data was used to derive the tidal constituents. Since the tidal signal is relatively small at the North Pole (M_2 amplitude varies between 5.3 and 6.1 cm among the gauges), the RMS differences and RSS differences between the interpolated tidal signal and bottom pressure gauges for the eight major tidal constituents range only from 1.2 to 2.3 cm, with HAM12 and FES12 having the smallest RSS. All other models have higher RSS due to large differences for individual constituents (K_1 for GOT4.8, OSU12, and TPXO8, and S_2 for DTU10).

5.2. Antarctic Seas

A total of 102 in situ measurements are available from seas surrounding Antarctica. Data sources include bottom pressure recorders; coastal tide gauges; and GPS, gravimeter, and tiltmeter measurements on the floating ice shelves [*King and Padman*, 2005; *King et al.*, 2011a, 2011b]. All derived tidal constituents, along with information about record length, measure type, and references are included in the Antarctic Tide Gauge Database (http://www.esr.org/antarctic_tg_index.html). The gravimeter and tiltmeter records are expected to be less reliable, generally being based on shorter and older records and a greater number of uncertain corrections used in the reduction. Unfortunately, the gravimeter records make up a large fraction of the Ross Ice Shelf records. However, the tide gauges are generally quality controlled. To verify this, the identical comparison between models and gauges to that for the Arctic Ocean was performed.

The maps of vector differences between interpolated and observed M_2 signals (Figure 6) suggest that, especially in regions covered by the large ice shelves, all models have problems in producing the correct tidal signal. All the models show vector differences larger than 10 cm on the Filchner-Ronne Ice Shelf, where the amplitude of M_2 exceeds 1 m. Similarly, on the Ross Ice Shelf, all the models except HAM12 and TPXO8 have vector differences for M_2 exceeding 10 cm, representing a substantial relative error as the amplitude is less than 30 cm. However, the gravimetry data here are less reliable.

The calculated RMS differences between in situ measurements and model predictions are listed in Table 7. Because OSU12 is not available on the ice shelves, it is excluded from this comparison. The RMS differences for the full set of common gauges are 3–4 cm, 2–5 cm, 2–6 cm, and 1–5 cm for the M_2, S_2, K_1, and O_1 constituents, respectively. Most models have large RSS on the Larsen C and Filchner-Ronne ice shelves in the Weddell Sea. TPXO8 exhibits the lowest RMS for most constituents and clearly the lowest overall RSS, consistent with its assimilation of many of these in situ data records.

Table 7 also shows the average constituent amplitude over the tide gauges. In contrast to the Arctic Ocean, amplitudes of the K_1 and O_1 constituents around sections of Antarctica can be large; the four major constituents, M_2, S_2, K_1, and O_1 display roughly similar amplitudes around Antarctica (although this assessment is influenced by the irregular distribution of the in situ data). For the five models that do not assimilate data, i.e., HAM12, FES12, EOT11a, DTU10, and GOT4.8, the mean RMS error for M_2 is 17% of the M_2 average amplitude. This RMS error increases to more than 20% for most other constituents, with a value of nearly 30% for the smaller N_2 tide.

To illustrate the magnitude of the misfit, Figure 7 compares GPS-based elevations [*King et al.*, 2011a, 2011b] with model time series for the two sites FR03 and FR09 located on the Filchner-Ronne Ice Shelf in the Weddell Sea. Ocean tide loading displacement and atmospheric pressure ("inverse barometer") effects have been removed from the GPS time series, leaving a relatively smooth time series dominated by ocean tides. Tidal-band differences of several tens of centimeters are evident over the time window and vary substantially in amplitude and phase between models; such differences, and larger ones, are common to all GPS sites on the Larsen C and Filchner-Ronne ice shelves. In contrast, *Kim et al.* [2011] and *Oreiro et al.* [2014] report model-data differences for other Antarctic regions that are much smaller than those shown here,

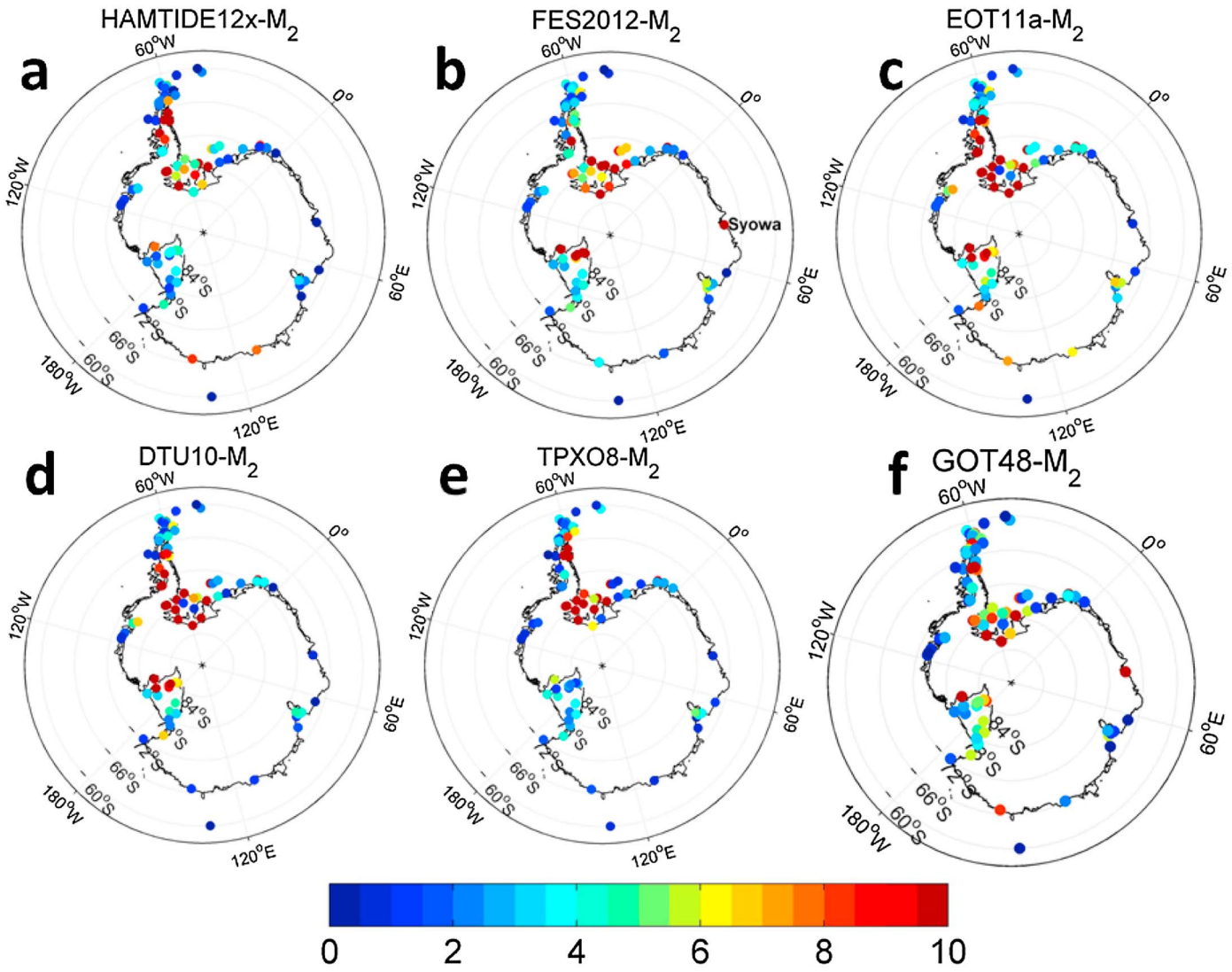

Figure 6. Magnitudes of vector differences (in cm) between in situ and interpolated M_2 tide amplitude for 86 sites that could be used by all models except for the OSU12, which excludes Antarctic ice shelves from its domain and therefore is not shown.

although some of the models they test are the same as those that we use here. These results highlight large spatial differences in tide model accuracy, in part depending on distance from altimeter-based model constraints, complexity of the local coastline, and water depth errors especially under large ice shelves. We note that *King et al.* [2011a] investigated seasonal variation in the amplitudes of M_2 and O_1 in the Weddell Sea and found them to be negligible.

6. Tests of Modern Tide Models Against Satellite Data

Tide model tests against in situ data are primarily local tests that could be hampered by details of the bottom topography in the models or other uncertain local model parameters. Such tests can also be limited by the quality or sparseness of the in situ data, a particular concern in polar regions. Testing the impact of tide models against various kinds of satellite measurements provides some crucial complementary assessments. Some of these tests (e.g., the effect on satellite orbit perturbations) are limited to an indirect, integral, quality assessment, but these can still be useful and are in any event of interest to the space geodetic community. Such tests are reported in this section.

6.1. Satellite Tracking Tests

The orbits of artificial satellites are significantly perturbed by the gravitational effects of ocean tides [e.g., *Lambeck*, 1988]. Monitoring such orbital perturbations with precise satellite tracking measurements thus

Table 7. RMS and RSS Differences (Both in cm) Between the Interpolated Antarctic Tidal Signal and Common Tide Gauges[a]

	Q_1	O_1	P_1	K_1	N_2	M_2	S_2	K_2	
No. of Stations	36	49	37	48	37	49	48	36	
Signal	6.79	30.50	10.80	32.43	8.12	37.62	27.65	9.28	RSS
GOT4.8	0.88	3.52	1.04	4.01	0.94	3.80	3.49	0.74	7.64
DTU10	1.09	4.70	1.87	5.38	1.70	3.10	4.74	1.35	9.62
EOT11a	1.23	4.92	2.05	5.83	1.82	3.48	4.80	1.36	10.21
HAM12	0.78	2.55	1.37	3.36	1.06	3.20	3.26	0.96	6.58
FES12	1.50	4.55	1.78	4.63	1.06	4.27	4.53	1.13	9.42
TPXO8[b]	0.53	1.48	0.74	2.22	0.76	3.14	2.37	0.49	4.92

[a]The average amplitude (in cm) for each tidal constituents of the Antarctic is listed. The values are given for the largest common set of tide gauges to five of the models (excluding TPXO8).
[b]Denotes a model that assimilates a subset of the selected in situ measurements.

provides an independent method to assess accuracies of global tidal models. The following subsections describe two complementary types of tracking: ground to satellite and satellite to satellite. For the former we use satellite laser ranging (SLR) from ground observatories; for the latter we use microwave range rates between the two Gravity Recovery and Climate Experiment (GRACE) satellites. Owing to the inherent limitations of spaceborne gravity measurements, both are sensitive only to long-wavelength components of tidal mass variations. The GRACE satellites are sensitive primarily to scales above 400 km [*Rowlands et al.*, 2005]. SLR is sensitive to only a few low-degree spherical harmonic components, generally of order 1 for diurnal constituents and order 2 for semidiurnal constituents.

To analyze the tidal residuals in either type of satellite tracking data requires gravitational models of nontidal variability which are as complete as possible. For the tests below, similar background models were used, including GRACE-based models of the static and time-variable gravity field and models of rapid atmospheric variability implied by operational models of the ECMWF. The GRACE tests also used models of ocean and continental hydrological variability, and they used higher-degree expansions for all fields. In all cases the body tides were modeled following 2010 Conventions of the International Earth Rotation and Reference Systems Service.

Each tested tide model was expanded into spherical harmonic series. Only the five major constituents M_2, S_2, N_2, O_1, and K_1 were used for each model, with 25 other minor tidal constituents (or in some cases, tidal groups) based on GOT4.8, except for long-period tides which were based on either TPXO6.2 or on

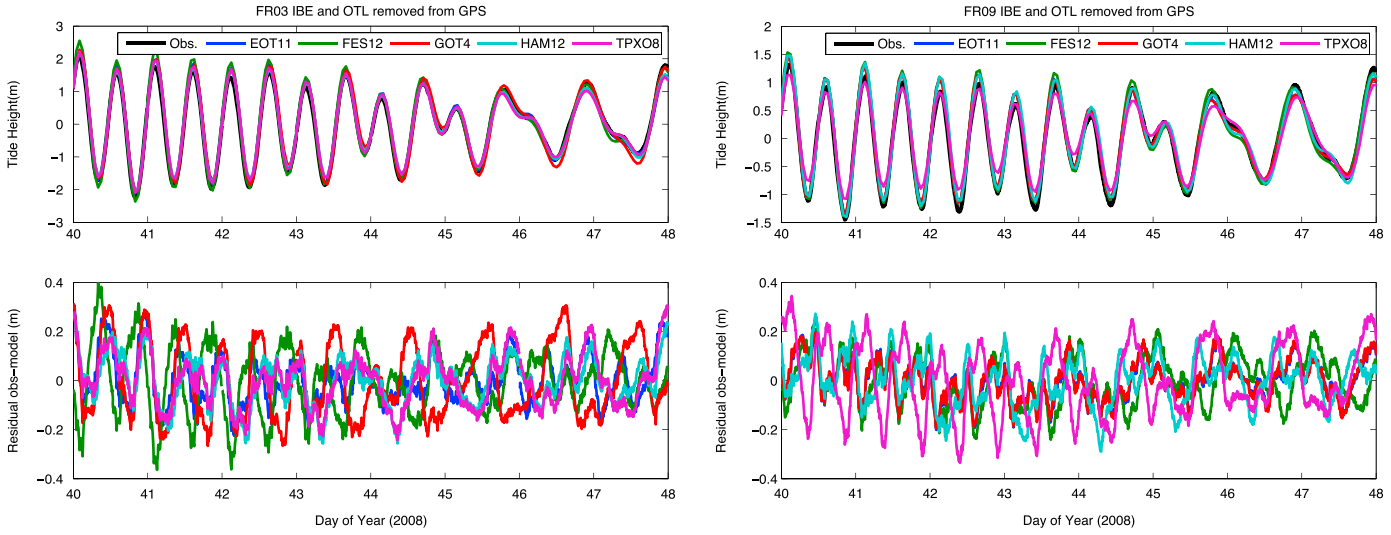

Figure 7. Comparison of GPS-based elevations [*King et al.*, 2011a, 2011b] with model time series for the two sites FR03 and FR09 located on the Filchner-Ronne Ice Shelf in the Weddell Sea.

self-consistent equilibrium models. Nodal and perigee modulations of lunar tides were accounted for by standard methods. For GRACE the degree of expansion was taken to 90; for the SLR satellites, to 20. The computation of the gravitational potential from the ocean tide expansions accounts for crustal loading [e.g., *Lambeck*, 1988, equation (6.1.24)], requiring an adopted set of loading Love numbers k'_n. The same computation requires knowledge of seawater density, which we took as a constant of $\rho = 1031\ \mathrm{kg\,m^{-3}}$.

6.1.1. Satellite Laser Ranging Tests

The impact of individual tide models on satellite orbit computations was tested against precise SLR tracking data from four geodetic satellites orbiting at a variety of altitudes and inclinations: Lageos, Starlette, Stella, and Larets. All four satellites are heavy, "cannonball," geodetic satellites covered with cube corner reflectors. For all four satellites we undertook a consistent set of analyses based on 261 seven-day orbital arcs over the period 2004–2008. Many SLR analyses estimate empirical acceleration adjustments at resonant frequencies (e.g., once per revolution) to accommodate force model errors; however, these kinds of adjustments potentially dilute the sensitivity to tidal perturbations in the orbit, so we here avoided such adjustments. The metric of this test is to identify the tide model that produces orbits with the smallest SLR tracking residuals.

Because SLR tracking is not continuous in time but rather relies on occasional satellite overpasses of the laser observatories, the SLR data are sensitive essentially to only long-period perturbations in satellite orbits. These perturbations depend on the orbital elements of a satellite, so each satellite is more sensitive to some tidal constituents than others. We therefore should not expect results to be completely consistent among the four satellite tests. For example, Starlette, specially designed for sensing tidal perturbations, is most sensitive to K_1, and then (in order) S_2, M_2, and P_1, with the K_1 perturbations having periods near 90 days [*Williamson and Marsh*, 1985]. Lageos is also sensitive to K_1, K_2, and S_2, but the K_1 periodicities are near 3 years and therefore potentially confounded by nontidal mass variations [*Lambeck*, 1988; Tables 6.8]. Lageos is also at far higher altitude than the others and is therefore sensitive to only the very lowest degree gravitational terms. Both Stella and Larets are in near-Sun-synchronous orbits.

Table 8 presents the mean RMS residuals in SLR tracking data for seven tested tide models, all of them modern altimetric-based models except—to assess historical progress—the old NSWC [*Schwiderski*, 1979] model. Each entry in the table gives the mean RMS over the 261 arcs, with the quoted uncertainties being the standard errors in those means. For each satellite the NSWC model clearly, and reassuringly, yields the largest SLR residuals. As an overall assessment of the SLR tests, Table 8 suggests that models EOT11a, HAM12, and GOT4.8 all perform well for all four satellites. TPXO8 is especially good for Starlette but appears slightly less accurate for the two Sun-synchronous satellites. The OSU12 model yields less accurate computed orbits, probably because it lacks tidal data under Antarctic ice shelves (cf. results in next section).

6.1.2. GRACE Tests

Satellite-to-satellite ranging data in GRACE are continuous in time, so (unlike the SLR test) GRACE data are sensitive to both short-period and long-period perturbations in the orbits. For a given mass anomaly of sufficient size, GRACE perturbations can be localized over that mass, which of course is the source of its great value for monitoring mass changes [*Tapley et al.*, 2004]. Our GRACE tests are based on the semiqualitative approach described by *Ray et al.* [2009]. Using similar, but more complete, background models as described above for the SLR tests, with higher-degree tide expansions, we have computed GRACE range rate residuals for the 7 year period 2004–2010. The processing of the range rate data follows steps described by *Luthcke et al.* [2006].

The entire processing was repeated for each tested tide model. These range rate residuals were then differentiated along track and low-pass filtered to generate range acceleration residuals, and these residuals were then binned into small geographical areas and tidally analyzed—see *Ray et al.* [2009] for further details. Regions displaying significant tidal energy in the residuals suggest regions of likely errors in the tested model. The test, however, is qualitative because the final maps are still in terms of GRACE measurement residuals and not in terms of tidal elevations of the sea surface, which would require an additional inversion to determine (for recent attempts at such inversions, see *Han et al.* [2007] and *Killett et al.* [2011]). Moreover, the signature of a mass anomaly in range acceleration includes significant sidelobes [e.g., *Ray et al.*, 2009, Figure 1], which act to extend anomalous regions over wider areas, including over land; this point must be kept in mind when interpreting our maps.

Tidal amplitudes of GRACE range acceleration in units of $\mathrm{nm\,s^{-2}}$ are shown in Figures 8–11 for constituents M_2, K_1, O_1, and S_2, and the global means of these residual amplitudes are tabulated in Table 9. Figure 8 (M_2)

Table 8. Mean RMS (cm) of Satellite Laser Ranging Residuals to Four Geodetic Satellites[a]

	Lageos-1	Stella	Starlette	Larets
NSWC	1.447 ± 0.021	4.819 ± 0.011	5.179 ± 0.009	5.040 ± 0.011
GOT4.8	**1.231** ± 0.020	**2.875** ± 0.007	3.043 ± 0.006	**3.263** ± 0.009
OSU12	1.259 ± 0.020	3.714 ± 0.009	3.675 ± 0.008	3.798 ± 0.010
EOT11a	**1.235** ± 0.020	2.991 ± 0.007	3.135 ± 0.007	3.341 ± 0.009
HAM12	**1.229** ± 0.020	3.025 ± 0.007	3.061 ± 0.006	**3.268** ± 0.009
FES12	**1.238** ± 0.020	3.203 ± 0.008	3.177 ± 0.007	3.449 ± 0.010
TPXO8	**1.227** ± 0.020	3.157 ± 0.008	**2.993** ± 0.006	3.599 ± 0.011

[a]Tabulated RMS for each satellite is the mean of the RMS residuals computed for each of 261 seven-day arcs over the period 2004–2008. Quoted uncertainties are standard errors in these means. Bold font marks models within 1 standard error of the smallest RMS, for each constituent. DTU10 model was not used in this comparison.

shows the expected high-latitude problems, where the tide models are known to be less accurate owing to the lack of satellite altimetry. In addition, however, the resolution of GRACE is sufficiently high to allow us to resolve relatively isolated, near-coastal anomalies in lower latitudes. For example, EOT11a displays small M_2 anomalies along western India, whereas HAM12 (which assimilated the EOT11a tides) has mostly corrected these problems. Most models (except TPXO8) show small anomalies along the coast of British Columbia. These figures can therefore guide modelers to locations where improvements may be needed.

Nevertheless, it is also possible that some anomalies shown in Figure 8 reflect GRACE (or GRACE processing) errors and not tide model errors. For example, all six models show anomalies near New Zealand, where the M_2 wave is large and of relatively short wavelength as it rotates around the islands; our use of a spherical harmonic series limited to degree 90 may be inadequate to capture the full M_2 signal near New Zealand. The large anomalous regions of the North Atlantic may also—given that all six models are similar—represent systematic errors in GRACE processing. For example, errors in the adopted density of seawater in regions of large-amplitude tides, such as off western Europe, may be partly to blame—see Figure 10 of *Ray et al.* [2009].

Figure 9 emphasizes that all models have significant errors around Antarctica. The extent of the errors in TPXO8 may be somewhat misleading, owing to sidelobes of the main anomaly, especially in the Ross Sea. Sidelobes are also suggested in the HAM12 panel in the western Ross Sea. Because EOT11a defaults to FES2004 in high latitudes, Figure 9 suggests that FES2004 was more accurate than FES12 in the Arctic K_1. Similarly, Figure 10 (O_1) suggests that FES2004 is more accurate than FES12 in the Weddell Sea, but the reverse is true in the Ross Sea, where FES12 appears to be the most accurate of all six models.

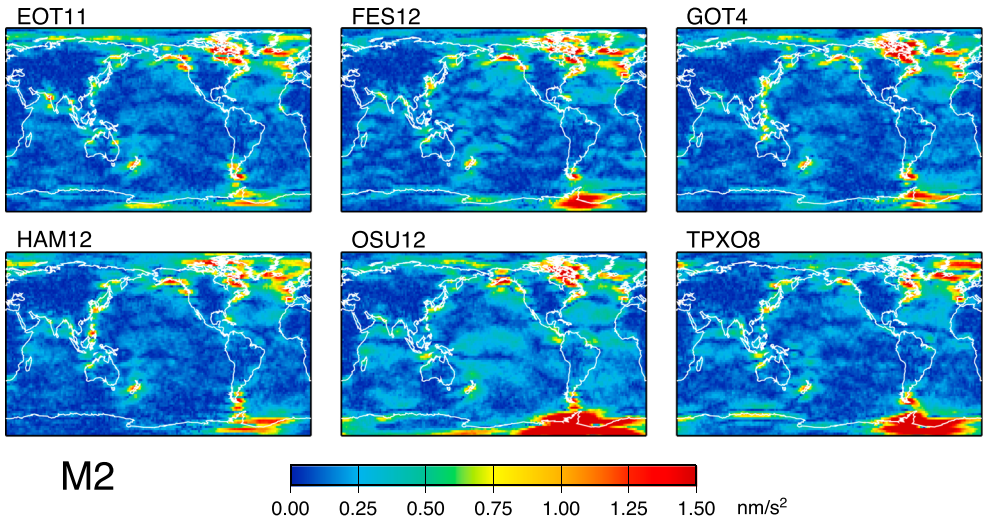

Figure 8. Amplitudes at the M_2 tidal frequency in 7 years of GRACE range acceleration residuals, based on six different tidal models. Locations showing significant amplitudes suggest errors in the corresponding tide model.

Table 9. Mean GRACE Range Acceleration Residual Amplitudes (nm s^{-2}) at Tidal Frequencies

	M_2	S_2	O_1	K_1
NSWC	1.237	0.610	0.269	0.426
GOT4.8	0.198	0.161	0.090	0.135
OSU12	0.267	0.190	0.168	0.197
EOT11a	0.194	0.161	0.079	0.132
HAM12	0.195	0.165	0.032	0.146
FES12	0.206	0.192	0.092	0.172
TPXO8	0.212	0.166	0.107	0.172

The OSU12 model performs noticeably poorly around Antarctica in all constituents for one obvious reason: the model does not include regions under the permanent Antarctic ice shelves. Tides in those regions are generally very large (although M_2 is small under the Ross Ice Shelf), so neglecting these regions will induce significant residuals in GRACE ranging data. The same error has also undoubtedly contributed to OSU12's somewhat higher SLR residuals shown previously in Table 8.

In S_2, shown in Figure 11, the overall background of the residuals is high, especially when compared with the very quiet O_1 residuals. The noise is likely induced by various systematic errors related to the GRACE orbit plane alignment with the Sun (so-called β' errors); the orbit plane precession period is identical to the S_2 alias period. In addition, in low latitudes, errors in the S_2 atmospheric tide contribute but only to the extent that errors are identical in all six panels. In fact, altimeter-based models themselves tend to display β'-like errors; *Ray* [2013] discusses several of these, including errors in most models from inadequate air tide modeling in the T/P dry-troposphere correction and the lack in all models of a correction for crustal loading by the S_2 air tide. (We note that a small anomaly in all panels over the Amazon basin is caused by an error in the adopted hydrological model which occurs at the 161 day S_2 alias period.)

Both Table 9 and Figures 8–11 suggest that the HAM12 model may be the best for processing GRACE range rate data, with EOT11a and GOT4.8 close behind. We note that TPXO8, which appears perhaps the best in lower latitudes, has relatively large errors over the Weddell and Ross Seas; this is surprising since TPXO8 is the only model that assimilated a large number of in situ data in those regions. It is possible that some of those in situ data, such as old gravimeter stations on floating ice, may be problematic because of errors in ocean loading [*King and Padman*, 2005] or errors in instrument tilt. The new GPS data reported by *King et al.* [2011a, 2011b], including those data shown in Figure 7, were not assimilated into TPXO8 (or any other model), so future improvements in some of these problematic regions highlighted by GRACE should be forthcoming.

6.2. Satellite Altimeter Tests

Variance reduction tests on altimetric sea level anomalies constitute a standard method for evaluating ocean tide models. Tests of our seven primary global models are discussed in this section.

Each tested ocean tide model was separately employed to generate corrections to sea level anomalies from a number of different satellite missions. In each case we have used the eight major tidal constituents (M_2, S_2, N_2, K_2, K_1, O_1, P_1, and Q_1), with all long-period constituents held fixed and other constituents (e.g.,

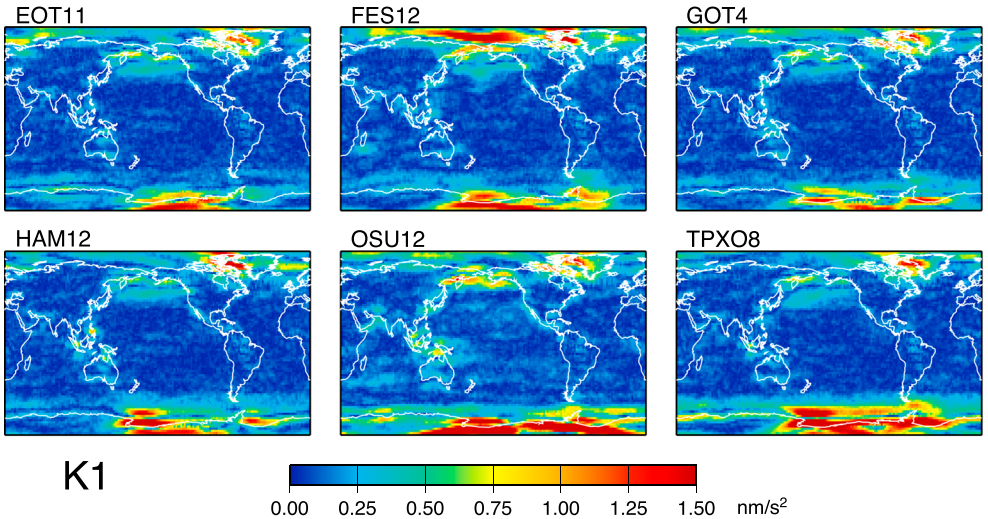

Figure 9. As in Figure 8 but for the K_1 frequency.

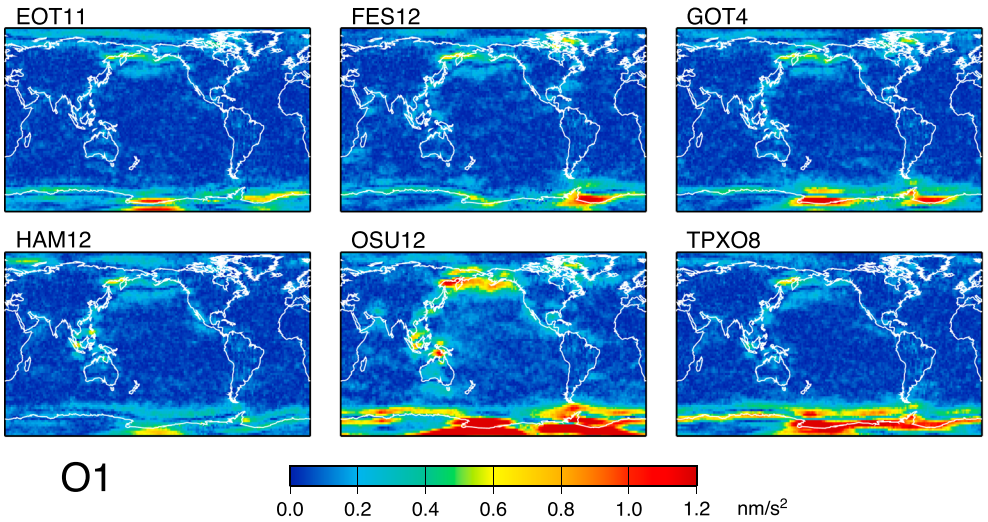

Figure 10. As in Figure 8 but for the O_1 frequency.

MS_4) ignored. This is admittedly not an optimum approach, because it ignores the compound tides that are included with some of our tested models (e.g., FES2012 is distributed with seven compound tides). Thus, our tests of these models in shallow water will yield residual variances somewhat inflated from what the complete models would presumably have yielded. However, the approach does allow consistent testing of the major constituents with identical software.

In addition to the tide corrections the altimetric data were processed with standard sets of media, instrument, and geophysical corrections. These include a dynamic atmospheric loading correction via the MoG2D (2-D Gravity Wave Model) [*Carrère and Lyard*, 2003]. An equilibrium model was used to correct for long-period tides, and the model of *Matsumoto et al.* [2000] was used for all load tides. Further detailed comparison methodologies are described by *Fok* [2012].

The satellite altimeter data used for these tests include Topex/Poseidon (10 day cycles 4–364), Topex Interleaved Mission (cycles 369–481), Jason-1 (cycles 1–259), Jason-1 Interleaved Mission (cycles 262–374), Jason-2 (cycles 1–184), and the Jason-1 Geodetic Mission (cycles 382–409); GFO (17 day cycles 37–223), Envisat (35 day cycles 10–94), and the Cryosat-2 (29 day cycles 1–40). Much of these data were, of course,

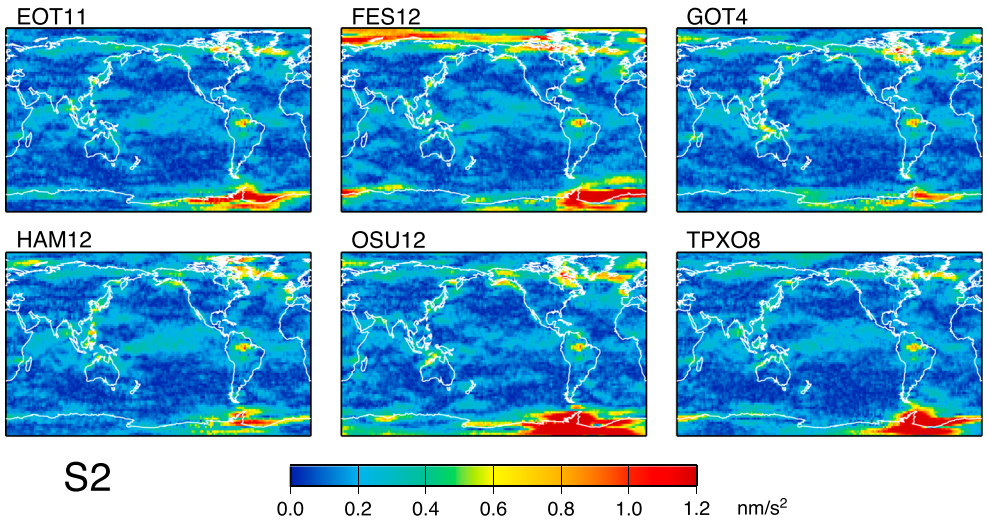

Figure 11. As in Figure 8 but for the S_2 frequency. The overall inflation of background noise stems from a multitude of possible β'-like errors in both GRACE data and in the ocean tide models themselves. Some signals, however, stem from inadequate modeling of hydrology, such as the small anomalies evident in the Amazon basin which may exist at the 160 day S_2 alias period for GRACE.

Table 10. Standard Deviations of Residual SSH Anomaly (in cm) Along Satellite Tracks in Shallow Oceans (Depth < 1000 m) After Applying Ocean Tide Model Corrections[a]

Model	T/P	Interlaced	GFO	Envisat	Jason-1 Interlaced	Jason-1	Jason-2	Jason-1 GM	CryoSat-2
GOT4.8	10.66	10.37	11.40	10.55	11.24	10.99	10.69	10.67	11.35
DTU10	10.66	10.34	11.45	10.51	11.18	10.95	10.67	10.67	11.30
OSU12	10.83	10.12	11.44	10.65	11.22	10.98	10.69	10.72	11.34
EOT11a	10.82	10.50	11.65	10.62	11.37	11.20	10.78	10.75	11.44
HAM12	10.72	10.47	11.72	10.76	11.34	11.15	10.68	10.67	11.44
FES12	10.69	10.34	11.52	10.59	11.09	10.96	10.62	10.61	11.29
TPXO8	10.82	10.54	11.74	10.84	11.44	11.17	10.78	10.77	11.58
Before	55.06	54.82	53.24	49.49	56.23	56.38	55.42	54.63	49.99

[a]The bottom line is the respective SSH standard deviation before ocean tide correction was applied.

employed in the development of the models but not all. For example, all models are independent of the Jason-1 geodetic mission data and all are independent of Cryosat-2 data. All the altimeter data used in this section were extracted from the Radar Altimeter Database System [*Scharroo*, 2008].

The overall statistics for the altimetry sea level anomaly tests as a function of ocean tide models are summarized in Tables 10 and 11 for shallow (< 1000 m water depth) and deep-ocean areas, respectively. One immediately notices that differences in variance among the different missions is generally greater than the differences among models within a mission. This likely arises because the various missions sampled the oceans at different times, and it also may reflect differences in data quality. In the deep ocean the residual altimeter variances are nearly indistinguishable between different tide models, although the OSU12 model is sometimes anomalous: it displays slightly better statistics on T/P-interlaced, GFO, and Jason-1 missions but slightly weaker statistics for other missions, while other models show similar values for all missions (within 0.05 cm).

Considering shallow-water regions, one can observe some differences between each tidal correction, although differences are still very small: FES12 and DTU10 lead to lower variance for six missions and GOT4.8 and OSU12 for four missions, while other models lead to slightly higher variance (differences of 0.05–0.42 cm). These results suggest that all seven models have comparably accurate determination of the main waves when averaged over the global ocean. Certainly there remain significant differences in some local/shallow-water regions as previously shown in the tide gauges tests of section 4, but these differences are for the most part evidently smoothed out by the global statistics of Table 11.

7. Elevation Errors of Purely Hydrodynamic Models

Although this paper is focused mostly on highly accurate data-assimilative global tide models, it seems both timely and enlightening to use the test machinery we have in place to examine also a suite of numerical models that do not assimilate any data at all. Such models are far less accurate than those that assimilate satellite altimetry, but they have nonetheless been improving significantly over the past decade. Improvements in purely hydrodynamic models have stemmed from higher spatial resolutions and better

Table 11. Standard Deviations of Residual SSH Anomaly (in cm) Along Satellite Tracks in Deep Oceans (Depth > 1000 m) After Applying Ocean Tide Model Corrections[a]

Model	T/P	Interlaced	GFO	Envisat	Jason-1 Interlaced	Jason-1	Jason-2	Jason-1 GM	CryoSat-2
GOT4.8	10.07	9.76	10.30	9.99	10.12	9.84	10.06	10.15	10.21
OSU12	10.13	9.60	10.23	9.97	10.32	9.76	10.16	10.34	10.44
DTU10	10.07	9.76	10.31	10.01	10.13	9.84	10.07	10.15	10.22
EOT11a	10.08	9.75	10.31	9.98	10.11	9.84	10.06	10.16	10.21
HAM12	10.07	9.80	10.32	10.00	10.12	9.85	10.06	10.13	10.19
FES12	10.10	9.78	10.32	9.99	10.13	9.85	10.07	10.15	10.21
TPXO8	10.09	9.80	10.34	10.02	10.13	9.87	10.07	10.14	10.21
Before	32.65	32.62	33.00	32.77	32.62	32.55	32.53	32.39	32.92

[a]The bottom line is the respective SSH standard deviation before ocean tide correction was applied.

Table 12. Differences (cm) of M_2 Elevations in NSWC and in Purely Hydrodynamic Models Versus Test Data[a]

	Deep Ocean		Shelf Seas	
	RMS_{TG}	RMS_{ALT}	RMS_{TG}	RMS_{ALT}
NSWC	4.27	4.41	—	17.4
HIM	8.75	5.25	33.7	22.3
OTIS-GN	7.54	6.76	25.3	18.6
STORMTIDE	8.33	7.76	48.2	27.9
OTIS-ERB	5.63	4.65	23.6	24.0
STM-1B	12.69	7.74	30.5	25.8
HYCOM	7.82	7.00	49.0	26.2

[a]RMS_{TG}, root-mean-square differences with BPR and tide gauge constants. RMS_{ALT}, root-mean-square differences with model TPXO8 over the entire ocean domain.

bathymetric data and also from better understanding of tidal dissipation—in particular from the realization that open-ocean conversion of barotropic tidal energy into baroclinic motion is a significant energy sink [*Egbert and Ray*, 2000]. As noted in section 2.3, all but one of the six forward models examined here account for this energy sink through a parameterized topographic internal wave drag; *Green and Nycander* [2013] discuss such parameterizations in some detail. Thus, recent improvements in hydrodynamic tide models represent in large part a better understanding of the ocean, and these advances deserve to be documented. We restrict our attention here to only M_2.

Table 12 summarizes comparisons of each forward tide model with the same sets of deep-ocean bottom pressure recorders and shelf water tide stations used in sections 4.1 and 4.2, respectively. As anticipated, all the tabulated differences for the forward models are much larger, by roughly a factor of 10, than corresponding differences for the modern models that assimilate altimetry. In light of this, for testing the forward models we may treat the assimilation models as "truth" and thereby obtain a more complete picture of the modeling errors, one not confined to a sparse tide gauge network. Thus, the corresponding RMS differences with TPXO8 have been added to Table 12. The tide gauge and TPXO8 statistics are not completely consistent in their ranking of models, probably owing to the geographic limitations of the gauge network, but they do generally agree on which models are most accurate and which are less accurate. The table entries suggest that the forward models HIM and OTIS-ERB are the most accurate in deep water, with OTIS-GN not far behind; OTIS-GN is the most accurate in shallow water, with HIM, STM-1B, and OTIS-ERB somewhat less accurate and the others trailing.

It is interesting to observe that some of the forward models are now starting to reach accuracies comparable to those of the pre-Topex era assimilative NSWC model of *Schwiderski* [1979], which from the late 1970s to early 1990s was generally considered the most accurate tidal model available. The RMS differences between NSWC and TPXO8 are 4.41 cm in deep water and 17.4 cm in shallow water, which is only slightly better than some of the entries in Table 12. For models that lack any data constraints other than bathymetry, to approach the NSWC accuracies does mark substantial progress in modeling.

Figure 12 shows the vector differences between each of the six forward models and TPXO8. To put these results into context, the vector differences between the altimeter-constrained TPXO8 and GOT4.8 models, as well as between TPXO8 and NSWC, are included in the figure. As was to be expected, the TPXO8–GOT4.8 differences are almost negligible in the deep ocean. Consistent with Table 12, the NSWC model is only slightly more accurate than some of the forward models. According to Figure 12 (we note its very nonlinear color bar), all six forward models have relatively large errors in the North Atlantic. This is consistent with the large M_2 amplitudes in that basin and the Atlantic's near-resonant response to the astronomical potential. OTIS-GN appears the most accurate there, with errors exceeding 10 cm only in the very high amplitude areas (e.g., Hudson Strait).

Three models do not include the ice-covered Ross and Weddell Seas, and all three are seen to have large errors extending throughout much of the Southern Ocean; HYCOM in particular seems sensitive to those missing seas. At one time tidal flexing of ice shelves was conjectured to be an important tidal energy sink, but it is now known that the entire Antarctic coastline accounts for less than about 50 GW of dissipation [*Ray and Egbert*, 1997; *Egbert and Ray*, 2001] or less than a few percent of the global total. Nonetheless, it seems evident that incorrect boundary conditions along that coastline are still capable of inducing modeling errors into far lower latitudes, so inclusion of these Antarctic seas seems critical for models that do not assimilate data.

8. Barotropic Tidal Currents

Comparisons of modeled tidal currents with observations are much less common than comparisons of modeled tidal elevations with observations, especially on basin and global scales. Among the basin- and

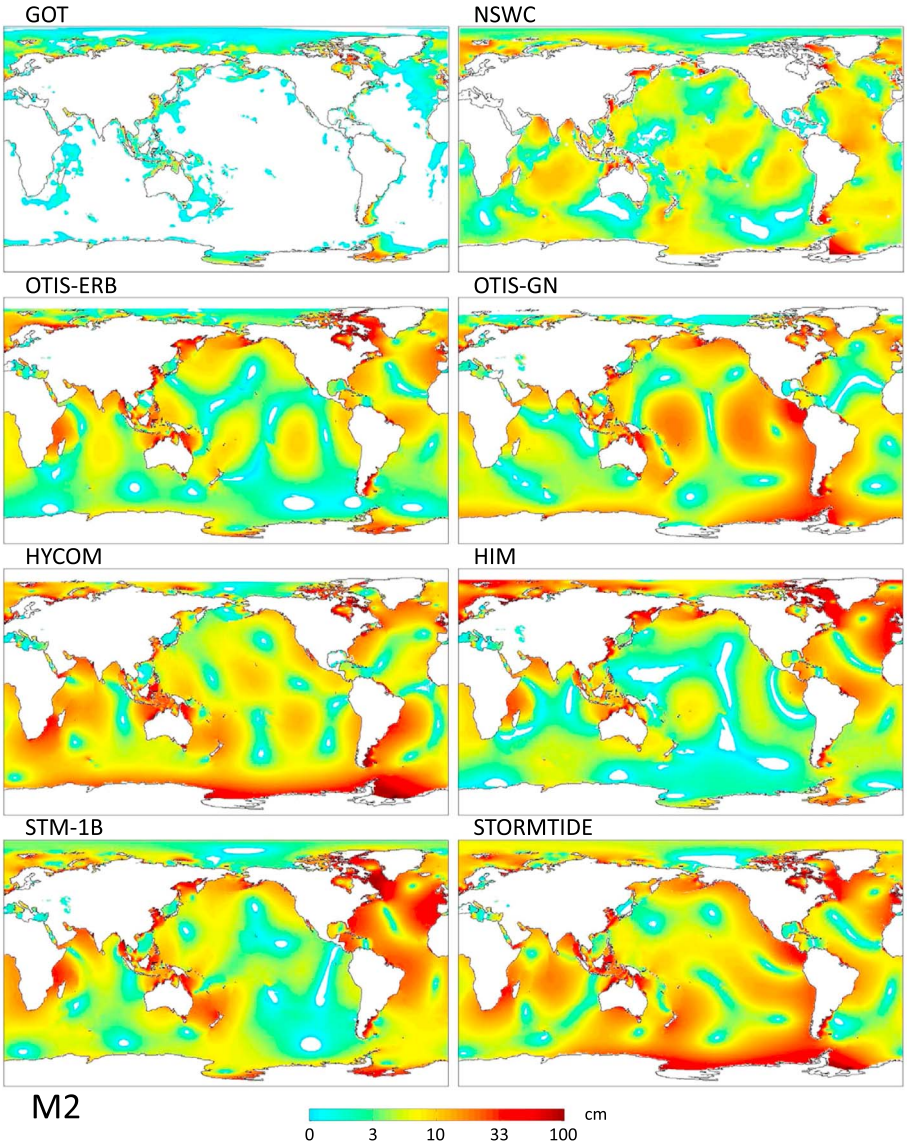

Figure 12. Absolute magnitudes (cm) of vector differences in M_2 elevations between TPXO8 and purely hydrodynamic ("forward") models identified by the labels in each panel. In the top row respective differences relative to GOT4.8 and NSWC are shown for reference.

global-scale studies that have been published, three representative examples are *Luyten and Stommel* [1991], who compared M_2 currents in moored current meter observations with those in the *Schwiderski* [1979] model; *Dushaw et al.* [1997], who compared currents from several tidal constituents in TPXO2.0 [*Egbert et al.*, 1994] to currents derived from acoustic tomography and from moored current meters; and *Ray* [2001], who deduced tidal currents from altimetrically derived tidal elevations and compared resulting currents with those derived from models, acoustic tomography, and moored current meters. All three of these studies focused on the barotropic component of tidal currents. *Timko et al.* [2012, 2013] compared fully three-dimensional (barotropic plus baroclinic) tidal currents in global eddy-resolving HYCOM with those in current meters. It should be noted that most barotropic tidal models do not solve for currents directly, so much as transports, from which currents are then derived. The accuracy of model currents depends on the accuracy of local seafloor topography employed for the model. As noted above, while some of the tidal models are constrained by observations of tidal surface elevation, none of the tidal models are constrained by measurements of tidal currents. While tidal currents are inherent to hydrodynamic models, some of the empirical models consider elevations only, with currents computed after the fact.

In this section, M_2 barotropic tidal currents from both data-assimilative models and forward models are compared against those derived from historical moored current meter records (section 8.1) and from acoustic tomography (section 8.2). The data-assimilative models used here are the TPXO8, GOT4.8, HAM12, FES12, and NSWC models. The forward models used here are the barotropic HIM, OTIS-ERB, OTIS-GN, and STM-1B models, and the baroclinic HYCOM and STORMTIDE models.

8.1. Tidal Currents From Moored Current Meters

The moored current meter records utilized here represent a subset of those employed by *Scott et al.* [2010] and *Timko et al.* [2012, 2013]. Because the present study focuses on barotropic tidal currents, we chose only moorings for which a meaningful vertical average might be computed. We required sampling at a minimum of once per hour, for 65 days, and at a minimum of three vertical levels, with at least one above 800 m and one below 1950 m. After excluding moorings with especially obvious measurement problems at small velocities (more below), or other apparent problems, a total of 56 moorings (Figure 13a) met these requirements.

The geographic sampling of tidal currents by moorings is very inhomogeneous given that mooring locations tend to focus on western boundary current regions, leaving large regions, such as the entire South Pacific, undersampled. Vertical coverage is also limited. Of the 56 moorings used here, 24 have only three current meters, 19 have only four, 8 have only five, and only 5 have six or more. The sparse vertical sampling of the moorings makes accurate estimation of the barotropic mode difficult, with considerable contamination from baroclinic modes, as noted in earlier studies [e.g., *Luyten and Stommel*, 1991; *Dushaw et al.*, 1997]. Indeed, some earlier studies [e.g., *Luyten and Stommel*, 1991], instead of estimating the barotropic mode directly, took the currents in the bottommost current meter of a mooring to represent the barotropic mode. The HYCOM simulations, with relatively high vertical resolution, will be used to estimate the sampling error in M_2 barotropic tidal currents computed from vertically sparse moored current meter records.

We separate the barotropic and baroclinic components of tidal currents at the mooring locations using standard linear dynamical modes $F_m(z)$, where m is a vertical mode index and z denotes depth. The modes are obtained from the internal wave Sturm-Liouville problem [e.g., *Gill*, 1982; *Wunsch*, 1975], written in terms of the Brunt-Väisälä buoyancy frequency $N(z)$ [*Gill*, 1982], and an internal wave frequency taken to be that of M_2. We take the baroclinic modes to begin with an index of $m = 2$ (for the first baroclinic mode); the barotropic mode $F_1(z) = 1$ at all depths. For each mooring location, $N(z)$ is computed from the nearest grid point of the climatological 2009 World Ocean Atlas [*Antonov et al.*, 2010; *Locarnini et al.*, 2010]. For HYCOM, $N(z)$ is computed from the model output itself. The vertical modes are obtained with a shooting method code (Glenn Flierl, personal communication, 1995), which yields results that are orthonormal to high precision.

We can write the zonal component u of either the moored current meter velocities or the HYCOM velocities sampled at the moored current meter vertical levels (referred to as "SAMPLED HYCOM" in what follows), as

$$u(z,t) = \sum_{m=1}^{K} \sum_{c=1}^{L} F_m(z) A_m^c f_c(t_{\mathrm{ref}}) \cos\left[\omega_c(t - t_{\mathrm{ref}}) + \chi_c(t_{\mathrm{ref}}) + v_c(t_{\mathrm{ref}}) - \phi_m^c\right] + \epsilon, \tag{4}$$

where t is time, t_{ref} is a reference time (i.e., the beginning of the first year of a mooring record), m is an index of vertical mode number, K is the total number of vertical modes employed including the barotropic mode, c is an index of tidal constituent (M_2, S_2, K_1, etc.), L is the total number of constituents used, $f_c(t_{\mathrm{ref}})$ and $v_c(t_{\mathrm{ref}})$ are respectively the constituent-dependent nodal modulations of amplitude and phase referenced to t_{ref}, ω_c is the frequency of constituent c, $\chi_c(t_{\mathrm{ref}})$ is the constituent-dependent astronomical argument referenced to t_{ref} [e.g., *Pugh*, 1987], and ϵ is a residual.

The mode- and constituent-dependent amplitudes A_m^c and phase lags ϕ_m^c are solved for with a linear least squares fit. In effect, we have extended standard tidal harmonic analysis to solve for vertical mode structure over all the current meters in a mooring. A similar problem is solved for the meridional velocity component v. We solved for the five largest tidal constituents ($L = 5$; M_2, S_2, N_2, K_1, and O_1) but found that the M_2 barotropic mode estimated from the above technique was not very sensitive to the inclusion of other constituents. We found a slightly closer agreement between the current meter and TPXO8 estimates of the M_2 barotropic tidal currents with two vertical modes in the mooring estimation than with three. In what follows we display results from a fit using only two vertical modes (barotropic and first baroclinic).

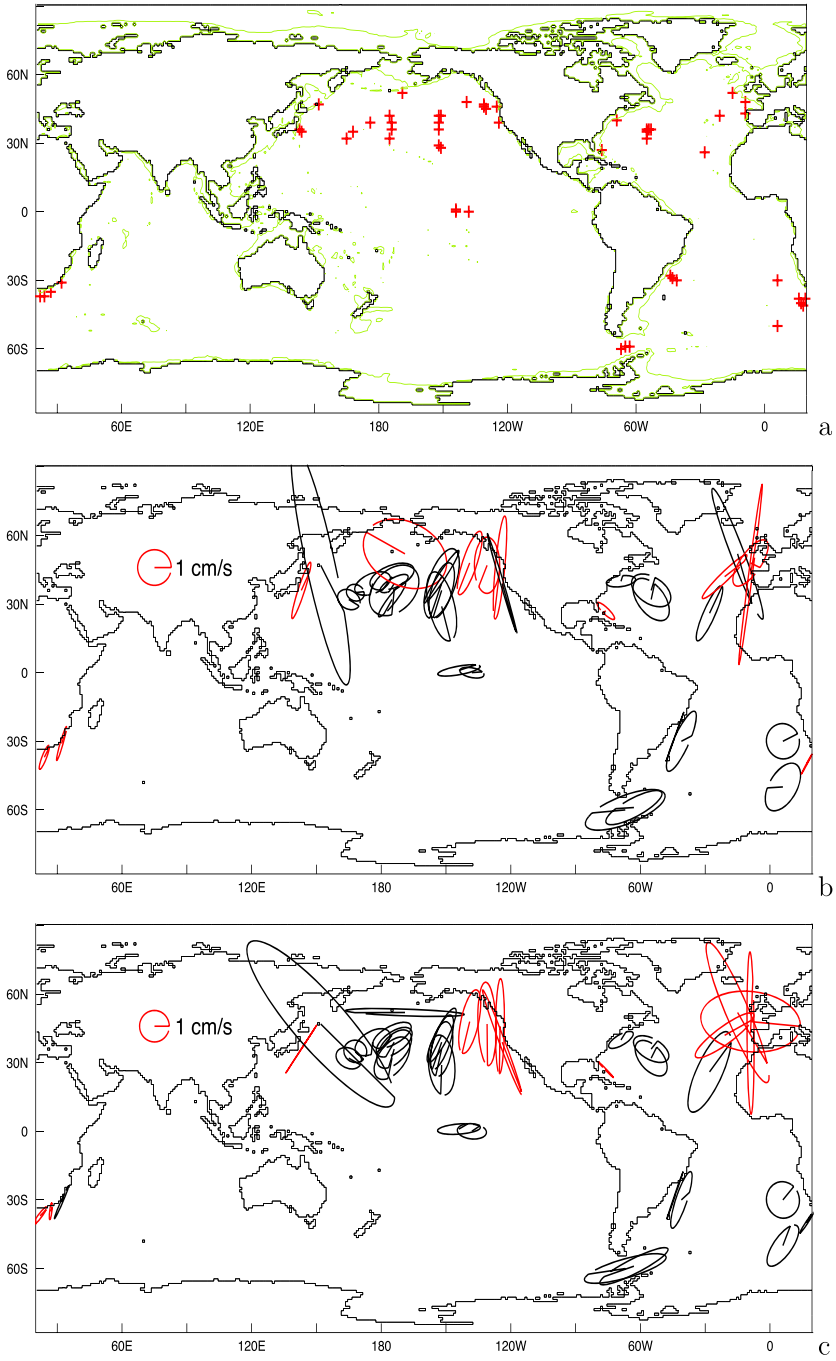

Figure 13. (a) Locations of 56 moorings used in the computation of M_2 barotropic tidal currents. (b) M_2 tidal ellipses inferred from mooring data. (c) M_2 tidal ellipses inferred from HAM12 at the mooring positions. In Figures 13b and 13c only 39 locations are shown to avoid clutter due to moorings located close to each other.

Figure 13b shows the M_2 barotropic tidal current ellipses computed from the moorings via the procedure above. Figure 13c shows the M_2 barotropic tidal current ellipses computed from the altimeter-constrained model HAM12. Visual comparison of Figures 13b and 13c indicates that there are many locations where the mooring and HAM12 estimates lie close to one another but also many locations where they do not. There are some locations where the currents are of large magnitude and are quite different in the two estimates. This suggests that relatively small numbers of outliers may control RMS statistics, in like manner to earlier discussions of model/tide gauge elevation differences.

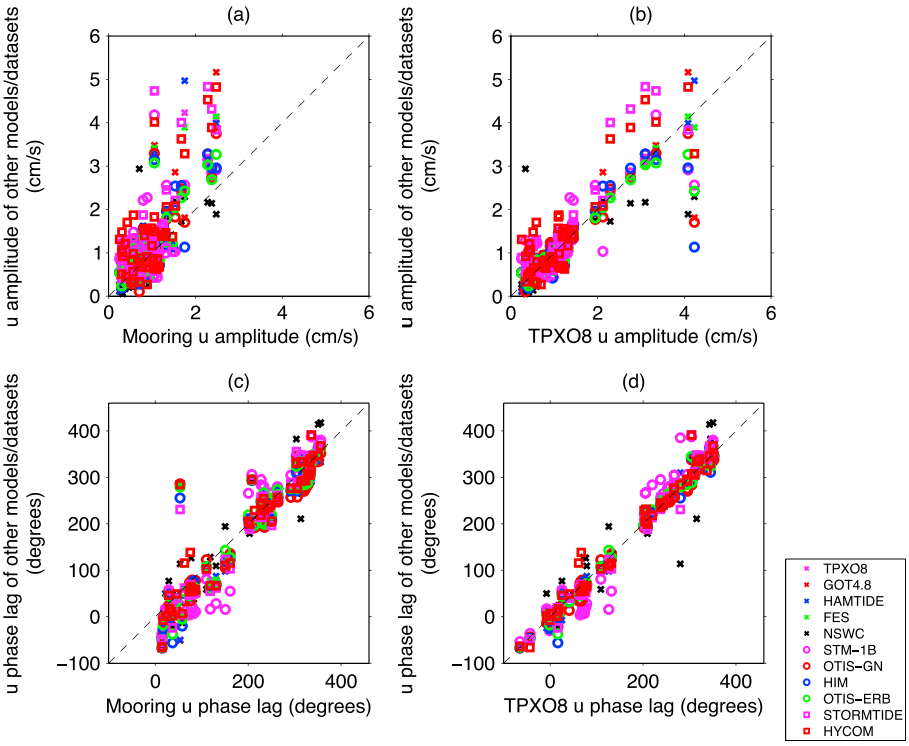

Figure 14. Scatterplots of (a, b) amplitudes and (c, d) phase lags of M_2 barotropic tidal zonal velocity component *u* at moored current meter locations shown in Figure 13, estimated from five different data-constrained barotropic tide models, four different forward barotropic tide models, and two different forward multilayer tide models forced by atmospheric fields in addition to the astronomical tidal potential, all plotted versus the mooring results (Figures 14a and 14c) and data-constrained model TPXO8 (Figures 14b and 14d). Values from data-constrained and forward barotropic models denoted by crosses and circles, respectively. Values from multilayer forward models denoted by squares.

Figure 14 shows the amplitudes and phase lags of the M_2 barotropic zonal velocity component (*u*) from the various assimilative and forward tide models, plotted against the mooring estimates (Figures 14a and 14c) and against the TPXO8 altimeter-constrained model (Figures 14b and 14d). For both amplitude and phase lag there is more scatter when models are plotted against mooring values than against TPXO8 values. This is consistent with previous work [e.g., *Dushaw et al.*, 1997; *Ray*, 2001], which concluded that tidal currents in different models often agree more closely with each other than with estimates made from moorings. The scatter in amplitude is somewhat larger than in-phase lag. The equivalent scatterplot for the meridional velocity component *v* (Figure 15) behaves similarly but shows somewhat less scatter than the *u* plots.

Because barotropic velocity consists of two (zonal and meridional) scalar components, we define the RMS velocity difference *D* between two different estimates as a quadrature sum of the RMS differences for each separate component; thus, the RMS velocity difference *D* is a two-component velocity equivalent of the RMS elevation difference which was used extensively earlier in the paper. As with elevations (see, e.g., Table 3) we compute a signal strength *S* alongside the RMS difference *D*; again, as with *D*, the velocity signal is a two-component equivalent to the elevation signal used earlier.

The RMS differences are computed against two standards, the moored current meter archive (CMA) and TPXO8. All resulting signals *S* and RMS differences D_{CMA} and D_{TPXO} are listed in Table 13. While the historic *Schwiderski* [1979] NSWC model has by far the largest signal *S*, values from all modern models lie relatively close together, ranging from 1.53 cm/s (OTIS-ERB) to 1.89 cm/s (STORMTIDE), a range of about 24%. Assimilative models lie in a tighter range, from 1.57 cm/s (GOT4.8) to 1.67 cm/s (HAM12)—a range of about 7%. Table 13 confirms that, consistent with discussions in previous studies, the signal in the moored current meters is slightly weaker than the signals in any of the models. *Luther et al.* [1991] and other sources discuss instrumental reasons (such as stalled rotors) that contribute to this tendency. Our own visual inspection of the bottommost current meter records in the CMA indicates that in approximately one third of the mooring locations examined, there are clear measurement problems at small velocities, consistent with stalled rotors.

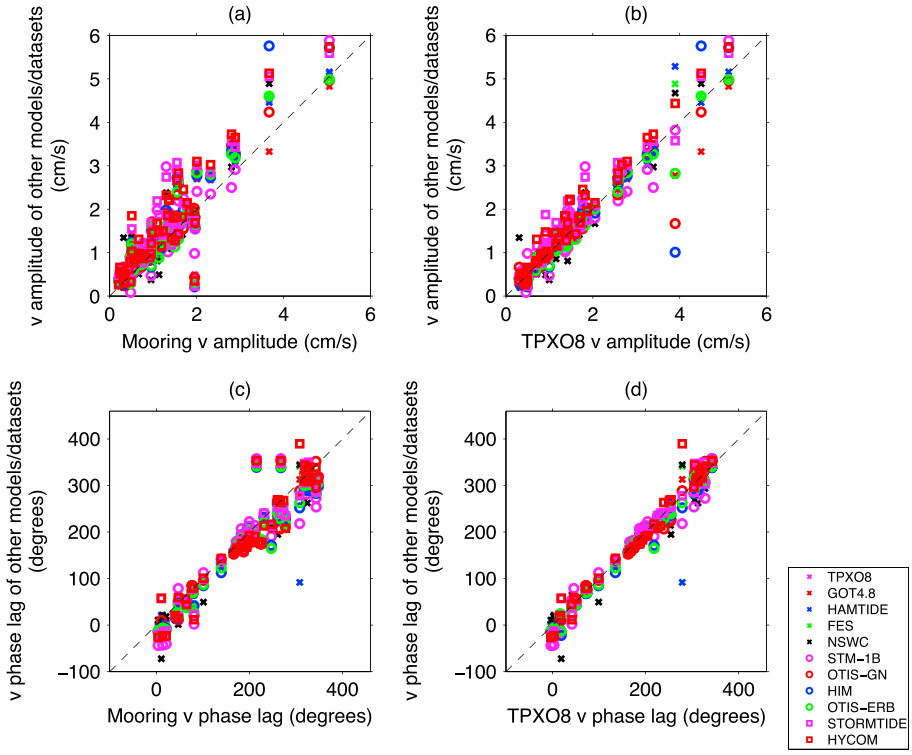

Figure 15. Same as Figure 14 but for meridional velocity component *v*.

The RMS difference of SAMPLED HYCOM versus fully vertically sampled HYCOM is 0.99 cm/s. This number roughly represents an error in barotropic mode estimation from sparse vertical sampling. We therefore cannot reasonably expect any of the models to agree with the CMA estimates at a level much lower than 0.99 cm/s. Indeed, the D_{CMA} values are of this order, generally a little less for modern assimilative models, a little more for modern forward models, and much more for the NSWC and SAMPLED HYCOM results. The

Table 13. Signals *S* and RMS Differences *D* of M_2 Tidal Currents (See Text for Definition), Averaged Over the Mooring Locations Shown in Figure 13[a]

Model or Data Set	Signal (cm/s)	D_{CMA} (cm/s)	D_{TPXO8} (cm/s)
Mooring data	1.45	–	0.83 (0.39)
Modern data-constrained models			
TPXO8	1.63	0.83 (0.39)	–
GOT4.8	1.57	0.87 (0.38)	0.32 (0.047)
HAM12	1.67	0.90 (0.38)	0.24 (0.049)
FES12	1.65	0.83 (0.40)	0.16 (0.086)
Historical Models			
NSWC	2.24	1.58 (0.38)	1.50 (0.23)
Purely hydrodynamic models			
HIM	1.59	1.07 (0.56)	0.65 (0.17)
OTIS-GN	1.56	0.98 (0.57)	0.47 (0.22)
STORMTIDE	1.89	1.18 (0.55)	0.62 (0.30)
OTIS-ERB	1.53	1.03 (0.51)	0.52 (0.20)
STM-1B	1.72	1.17 (0.64)	0.73 (0.54)
HYCOM	1.86	1.06 (0.67)	0.56 (0.38)
SAMPLED HYCOM	1.87	1.52 (1.07)	1.05 (0.84)

[a]RMS differences D_{CMA} and D_{TPXO8} are computed against the moored current meter archive (CMA) and against TPXO8, respectively. The RMS difference of SAMPLED HYCOM versus HYCOM is 0.99 cm/s. Numbers in parentheses are median D values.

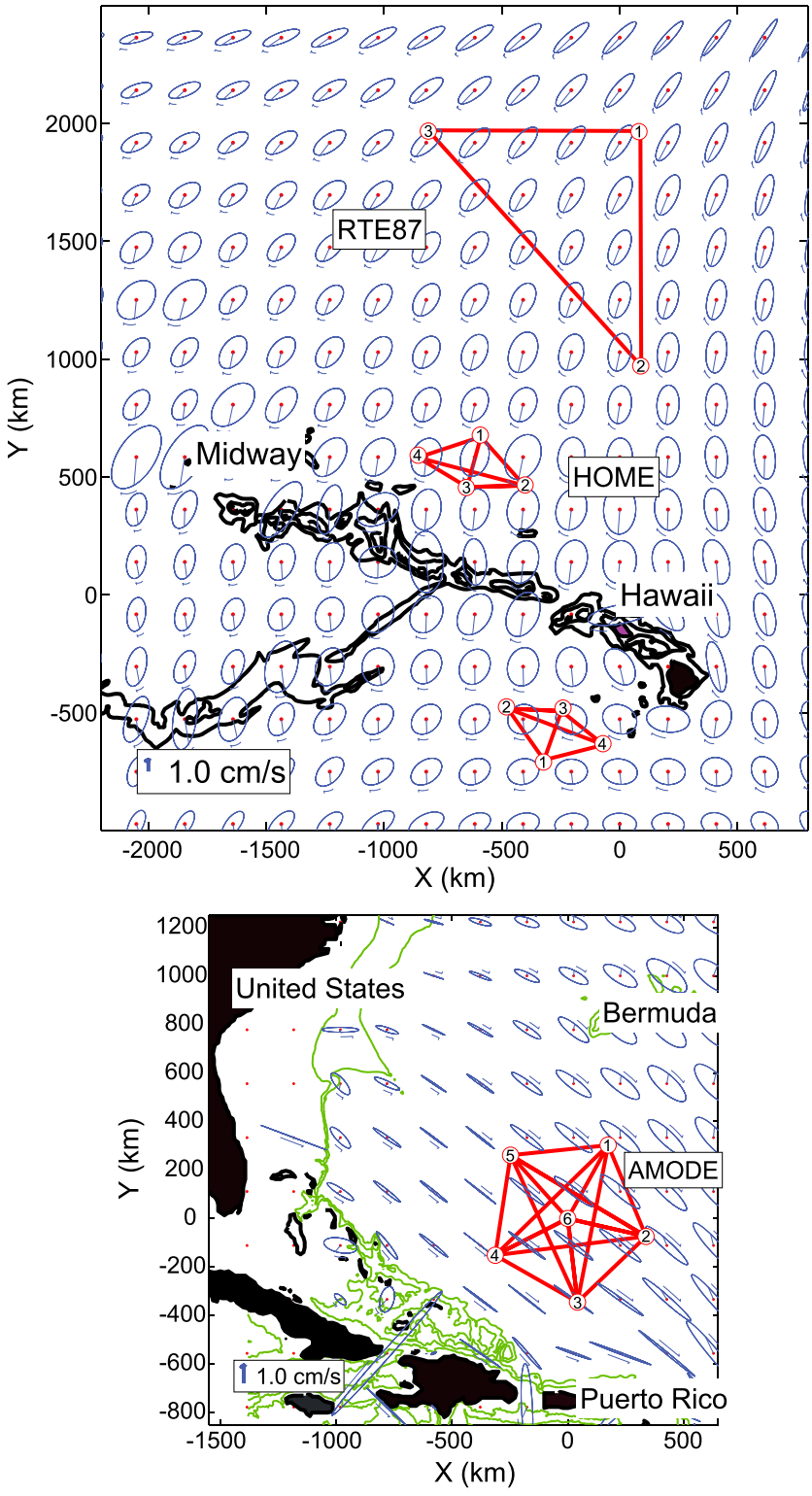

Figure 16. M_2 barotropic tidal current ellipses for (top) the central North Pacific and (bottom) the western subtropical Atlantic derived from the TPXO8 model. The RTE87 (1987), AMODE (1991), and HOME (2001) tomography arrays are indicated in red. Barotropic currents were estimated along these paths using reciprocal acoustic transmissions.

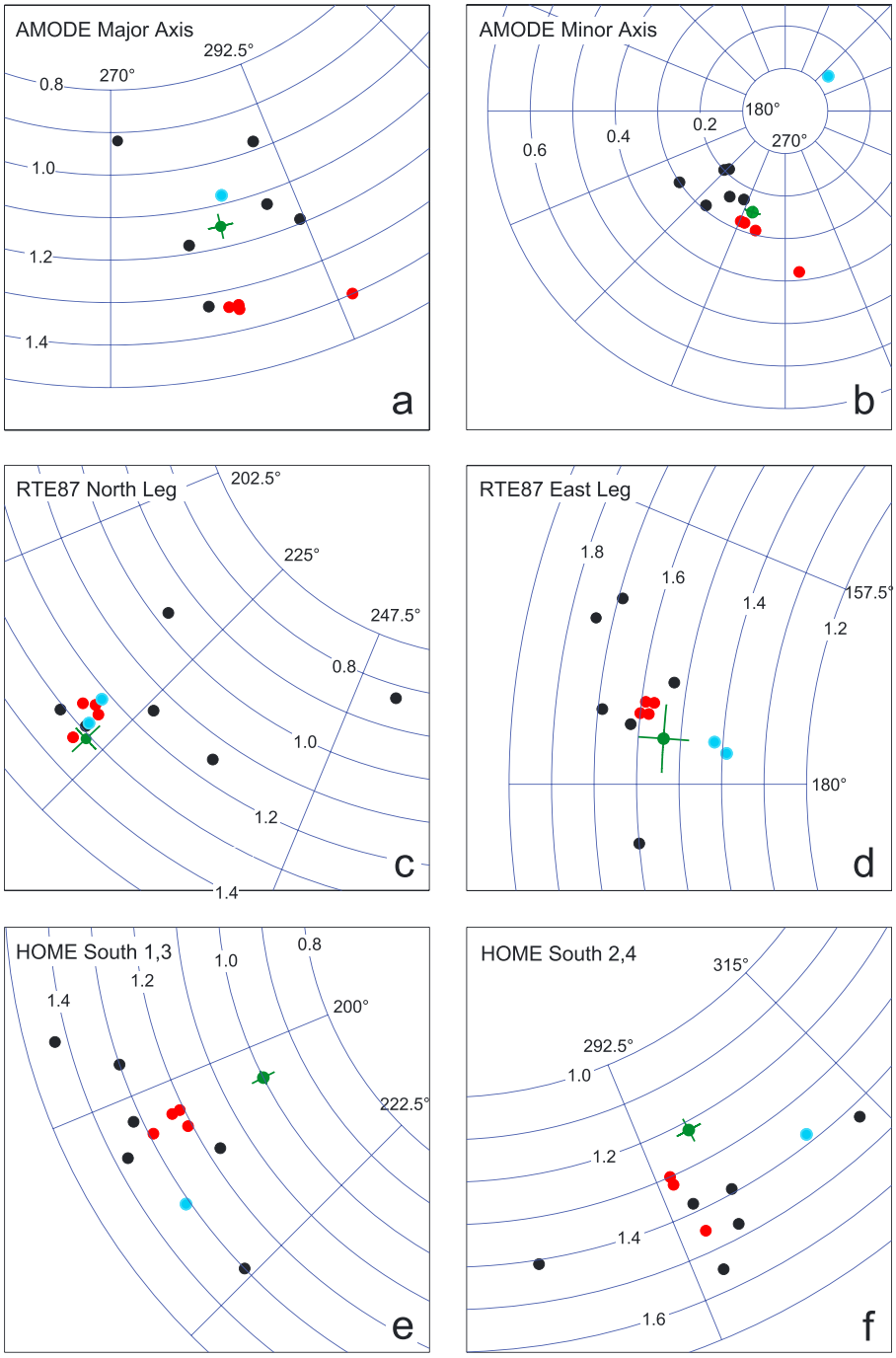

Figure 17. (a–f) Polar plot of M_2 tidal current amplitude and phase derived from various tide models (black: non-data-assimilating, red: assimilating, cyan: Schwiderski) as averages along the tomography paths indicated in each panel. Tomographic estimates are provided as green error bars (see Tables 14 and 15). Results for the Schwiderski model shown in Figures 17c and 17d were reported by *Dushaw et al.* [1995] and recomputed in this paper, respectively.

slightly lower D_{CMA} values for modern assimilative versus forward tide models suggest that the barotropic tidal current estimates made from moorings retain some minimal power to discriminate between the qualities of the two different types of models.

From the above it can be expected that the largest D_{TPXO8} values in Table 13 can be found for NSWC, SAMPLED HYCOM, and the current meter archive. The D_{TPXO8} values for all other models range from 0.16 cm/s (FES12) to 0.73 cm/s (STM-1B), smaller than the RMS differences found relative to the current meter archive.

Table 14. RTE87 Array: Tidal Current-Velocity Comparison, Amplitudes, and Phases[a]

	Path 3 → 1				*Path* 2 → 1				*Path*3 → 2			
	Amplitude (cm s^{-1})		Phase Lag (deg)		Amplitude (cm s^{-1})		Phase Lag (deg)		Amplitude (cm s^{-1})		Phase Lag (deg)	
	AT	TP	AT	TP	AT	TP	AT	TP	AT	TP	AT	TP
M_2	1.31 ± 0.03	1.24	223 ± 1	221	1.54 ± 0.04	1.57	176 ± 2	173	0.95 ± 0.07	0.97	131 ± 4	138
S_2	0.53	0.56	272 ± 4	272	0.56	0.63	207 ± 6	202	0.33	0.53	170 ± 14	163
N_2	0.14	0.16	191 ± 13	191	0.35	0.29	169 ± 8	163	0.16	0.16	111 ± 23	146
K_2	0.12	0.15	268 ± 13	269	0.15	0.18	184 ± 16	196	0.16	0.15	143 ± 20	158
O_1	0.43	0.45	101 ± 4	105	0.25	0.26	207 ± 9	204	0.13	0.30	255 ± 23	253
K_1	0.75	0.70	128 ± 2	125	0.41	0.39	216 ± 7	210	0.31	0.42	306 ± 13	273
P_1	0.18	0.22	132 ± 11	123	0.14	0.12	229 ± 21	208	0.07	0.14	171 ± 61	267
Q_1	0.10	0.08	64 ± 16	93	0.06	0.05	188 ± 34	202	0.11	0.06	217 ± 28	249

[a] AT and TP stand for acoustic tomography and TPXO8, respectively. Figure 16 shows the locations of the RTE87 moorings.

The RMS differences of modern assimilative models versus TPXO8 are significantly smaller than the RMS differences of forward models versus TPXO8. The smaller D_{TPXO8} values seen in modern models, both forward and assimilative, and the larger difference of the older NSWC model versus TPXO8 indicate a likely improvement, or at least convergence, over time of currents in modern tide models with the advent of satellite altimetry (for the assimilative models) and topographic wave drag schemes (for most of the forward tide models, STORMTIDE being the exception). It should be noted, however, that even the relatively small RMS differences of the modern assimilative tide models measured against TPXO8 represent relative errors (measured with respect to the signal *S*) of about 10–20%, much larger than, for instance, the 2% relative errors in M_2 elevations in modern assimilative models measured with respect to tide gauges (e.g., Table 3). The larger relative errors in tidal current estimates compared to tidal elevation estimates are another indicator of the greater difficulty in estimating and validating tidal currents as compared to tidal elevations.

Finally, we note that, as in the elevation comparisons discussed earlier in the paper, the median differences (given inside parentheses in Table 13) are lower than the differences defined as RMS values. In the case of the NSWC model, the median differences are much lower than the RMS difference; the large change seen in the two metrics is explained by very large differences at just two of the 56 locations. With this major exception, the general patterns seen in the RMS differences are also seen in the median values; the data-assimilative models perform better than the forward models, and the models lie closer to each other than to the mooring estimates.

8.2. Tidal Currents From Acoustic Tomography

Barotropic tidal currents are also measured by reciprocal acoustic tomography, which employs the travel times of acoustic rays that cycle throughout the water column and traverse *O* (500 km) ranges [*Dushaw et al.*, 1994]. The measurement is inherently integral over both depth and range and is not significantly influenced by baroclinic tidal currents. Previous comparisons of tidal current harmonic constants to tidal models have shown that tomography provides precise measurements of at least the first eight tidal constituents: M_2, S_2, N_2, K_2, K_1, O_1, and even P_1 and Q_1 [*Dushaw et al.*, 1995, 1997]. Our comparisons here will employ tidal currents determined from three experiments in the North Pacific and North Atlantic (Figure 16): (1) In the central North Pacific, tidal currents were measured along the three legs of the tomography triangle of the Reciprocal Tomography Experiment during summer 1987 (RTE87) [*Dushaw et al.*, 1995]. (2) The tomography arrays deployed in the vicinity of the Hawaiian Ridge in 2001 as part of the Hawaiian Ocean Mixing Experiment (HOME) [*Rudnick et al.*, 2003; *Dushaw et al.*, 2011] were intended to measure barotropic tidal currents with concurrent pressure measurements. The arrays were also designed to measure radiation of internal tides from the Hawaiian Ridge [*Dushaw et al.*, 2011]; hence, the longest path of the diamond-shaped arrays were parallel to the Ridge. (3) In the western North Atlantic, tidal currents were measured along each of the 15 legs of the Acoustic Mid-Ocean Dynamics Experiment (AMODE) tomography array in 1991–1992 [*Dushaw et al.*, 1997]. The AMODE array had path lengths of 350–660 km, 150–250 day record lengths, and measurements obtained every 3 h on every fourth day. The tomography and model estimates for tidal currents along several tomography paths are compared in Figure 17 and Tables 14 and 15. The figure shows only a selection of comparisons, and the tables include only a comparison relative to just the TPXO8 model due to space limitations.

Table 15. HOME Arrays: Tidal Current-Velocity Comparisons, Amplitudes, and Phases[a]

	South Path 1 → 2				*South Path* 1 → 3			
	Amplitude (cm s^{-1})		Phase Lag (deg)		Amplitude (cm s^{-1})		Phase Lag (deg)	
	AT	TP	AT	TP	AT	TP	AT	TP
M_2	1.09 ± 0.03	1.20	152 ± 2	149	1.00 ± 0.02	1.21	207 ± 1	208
S_2	0.42	0.51	182 ± 4	167	0.47	0.56	229 ± 3	230
N_2	0.20	0.22	163 ± 9	146	0.21	0.23	204 ± 6	207
K_2	0.12	0.14	182 ± 15	161	0.16	0.15	212 ± 7	224
O_1	0.14	0.19	236 ± 13	245	0.23	0.27	182 ± 5	178
K_1	0.17	0.17	239 ± 10	258	0.46	0.49	173 ± 3	178
P_1	0.07	0.06	317 ± 26	257	0.14	0.15	171 ± 8	180
Q_1	0.03	0.04	227 ± 59	240	0.04	0.04	275 ± 28	177
	South Path 1 → 4				*South Path* 2 → 3			
	Amplitude (cm s^{-1})		Phase Lag (deg)		Amplitude (cm s^{-1})		Phase Lag (deg)	
	AT	TP	AT	TP	AT	TP	AT	TP
M_2	1.15 ± 0.03	1.33	263 ± 1	264	1.18 ± 0.04	1.29	285 ± 2	278
S_2	0.61	0.61	280 ± 3	280	0.59	0.60	292 ± 4	294
N_2	0.27	0.27	264 ± 6	260	0.25	0.25	276 ± 9	273
K_2	0.16	0.17	276 ± 10	276	0.19	0.17	318 ± 13	290
O_1	0.33	0.29	133 ± 5	140	0.23	0.26	123 ± 10	127
K_1	0.49	0.54	166 ± 3	161	0.43	0.46	153 ± 5	154
P_1	0.12	0.16	143 ± 14	160	0.20	0.14	138 ± 12	153
Q_1	0.04	0.05	99 ± 46	124	0.09	0.05	14 ± 27	109
	South Path 2 → 4				*South Path* 3 → 4			
	Amplitude (cm s^{-1})		Phase Lag (deg)		Amplitude (cm s^{-1})		Phase Lag (deg)	
	AT	TP	AT	TP	AT	TP	AT	TP
M_2	1.22 ± 0.02	1.32	298 ± 1	294	1.33 ± 0.03	1.36	311 ± 1	309
S_2	0.55	0.58	311 ± 2	310	0.44	0.57	318 ± 4	327
N_2	0.23	0.25	286 ± 5	289	0.25	0.26	311 ± 8	303
K_2	0.14	0.16	308 ± 9	305	0.13	0.16	317 ± 15	322
O_1	0.21	0.23	113 ± 6	110	0.16	0.20	82 ± 12	87
K_1	0.30	0.35	113 ± 4	110	0.13	0.21	89 ± 14	124
P_1	0.11	0.10	157 ± 11	142	0.02	0.07	9 ± 108	120
Q_1	0.04	0.05	110 ± 32	93	0.09	0.04	33 ± 21	76
	North Path 1 → 3							
	Amplitude (cm s^{-1})		Phase Lag (deg)					
	AT	TP	AT	TP				
M_2	1.55 ± 0.02	1.67	10 ± 1	12				
S_2	0.73	0.76	38 ± 2	40				
N_2	0.30	0.30	12 ± 4	10				
K_2	0.25	0.21	28 ± 5	35				
O_1	0.21	0.25	354 ± 5	11				
K_1	0.32	0.44	350 ± 4	10				
v P_1	0.16	0.13	350 ± 7	10				
Q_1	0.03	0.04	13 ± 40	7				

[a] AT and TP stand for acoustic tomography and TPXO8, respectively. Figure 16 shows the locations of moorings.

In the North Atlantic, the harmonic constants derived from the AMODE paths along the major (Path 2, 5) and minor axes (Path 1, 4) of the tidal ellipses indicate that the comparisons between measured and model tidal harmonic constants are in general agreement (Figures 17a and 17b). Estimates from three of the four data-assimilating models are tightly clustered (the outlier is FES12), with variations in amplitude and phase of only *O* (0.05 cm/s) and a few degrees. Not surprisingly, models not constrained by data gave estimates with greater scatter but were still in agreement with the other models and tomography by *O* (0.1 cm/s) in amplitude and *O* (10°) in phase. With a measurement uncertainty of 0.02 cm/s and a difference of about 0.2 cm/s, the tomography amplitude along the major axis disagrees with the assimilation models by about 10 standard deviations. Except for the FES12 model, the M_2 tidal phases measured on all the tomography paths agree with those from the assimilation models within uncertainty.

In the North Pacific, harmonic constants for tidal currents from data-assimilating models are also tightly clustered, while harmonic constants from non-data-assimilating models are noticeably more scattered (Figures 17c–17f). In the central North Pacific, RTE87 tomography and data-assimilating models agree within measurement uncertainty (0.03 cm/s, 1 °). Near Hawaii (Figures 17e and 17f), however, systematic differences between measured and modeled harmonic constants (0.25 cm/s in amplitude and a few degrees in phase) are significant. As observed in the Atlantic, differences occur primarily in amplitude and not phase. We can offer no explanation for the differences between the M_2 harmonic constants estimated from tidal models and tomography at this time.

One way to test the self-consistency of harmonic constants and their uncertainties obtained from acoustic paths of a triangular tomographic array is to estimate tidal vorticity [*Dushaw et al.*, 1997]. By Stokes' theorem, integration of current around a closed loop is equal to the areal-average relative vorticity. For barotropic tidal currents, this relative vorticity is small, since barotropic currents are predominantly irrotational. The small vorticity of the tides is induced primarily by tidal elevation stretching the vortex lines, with lesser contributions through meridional flow (the "beta-v" term) and flow over varying topography. The AMODE tomographic array offers 10 triangles from which vorticity was computed [*Dushaw et al.*, 1997]. The relative vorticities computed in this way had amplitudes larger than those obtained from the models by a factor of about 3–4 and had fairly stable phases that led most models by 10–50°. Uncertainties were large at about 20%. This calculation indicates that the harmonic constants estimated on the various tomography paths are at least self-consistent with the formal estimates for their uncertainties. The estimated relative vorticity was larger than expected, however, suggesting that the systematic differences between tomography and tidal models may be caused by larger-than-expected rotational components to the tidal currents.

9. Summary and Outlook

As demonstrated in this study, the accuracy of tide models has improved substantially over the last 20 years. As an example, we find an RMS difference of M_2 tide models relative to pelagic bottom pressure stations of 0.51 cm which has to be compared with 1.64 cm reported by Shum97. However, about half of this apparent model improvement actually stems from improvements in the test data, highlighting the fact that even today a substantial effort needs to be spent on the observational in situ tidal data bases. (Our equivalent test of the best Shum97 model gives 0.92 cm, but this is still roughly twice the RMS of the best modern model.) Meanwhile, improvements of global models in shallow water have been very impressive, with M_2 differences falling from 23.0 cm to 3.5 cm (Table 4, bottom). In some cases we were able to identify, and sometimes correct, errors in historic tide gauge data by observing when model-gauge differences far exceed the spread in our ensemble of models.

According to our tide gauge and bottom pressure tests, the RMS accuracy of the best altimeter-constrained tide models is found for the M_2 constituent to be 0.51, 3.5, and 4.5 cm for pelagic, shelf, and coastal conditions, respectively. For the combined eight major tidal constituents, the root sum of squares is 0.89, 5.1, and 6.5 cm for pelagic, shelf, and coastal conditions, respectively. Note, however, that RSS and RMS values for shallow regions may be misleadingly pessimistic because they can be skewed high by just one or two difficult locations where the models are especially poor. This was emphasized by Figure 3, which shows that the errors at a majority of shelf locations are less than 2.5 cm in M_2 but that there are remaining locations where errors are much larger by many decimeters or more. Some of these error-prone regions are highlighted in Figure 1 but not always—for example, Zanzibar, Tanzania, was identified as a poor station for some models even though Figure 1 suggests that the east coast of Africa is not especially problematic. Thus, while our overall RMS values are likely a good assessment of model quality in the deep ocean, no single value is representative of the errors in shallow water; the models may be fairly accurate or may be very poor, depending on location.

The long-wavelength components of models tested by analyzing satellite laser ranging measurements and GRACE intersatellite ranging measurements confirm that none of the tested tide models substantially stands out in overall accuracy. Several of the modern models are of comparable quality for use in precise orbit determination. The GRACE data show that all data-constrained models are still imperfect on basin and subbasin scales and that no single model outperforms all other models, especially in high latitudes where insufficient high-quality tide information exists. Of the tested models, GOT4.8, HAMTIDE, and TPXO8 tend to

have the smallest RSS differences relative to in situ observations for the deep ocean. For shelf regions, FES12 and TPXO8 appear to perform best. Over the Arctic, DTU10 shows the lowest RSS values.

Assessing model accuracies of tidal currents remains problematic owing to the relative sparseness of in situ velocity measurements and the difficulty of isolating the barotropic mode in moored current meter measurements. Relative to moored current meter data, reciprocal acoustic tomography leads to estimates of harmonic constants that have much lower reported uncertainties, but unfortunately such measurements have been made in only a few locations. Nevertheless, both current meter and tomography comparisons show that our tested assimilation models consistently offer more accurate estimates for currents than do unconstrained models. We also observed small systematic differences between all M_2 models and the tomography data in the western North Atlantic and near Hawaii, with currents from models tending to be larger by 10–20%. No significant discrepancies were found between modeled and observed phases. An explanation for the amplitude differences awaits future studies. Increasing the number of in situ high vertical resolution current measurement records, which presently constitute a small data set, would improve our knowledge of barotropic (and baroclinic) tidal velocity fields.

While global ocean tide models have reached an impressive level of accuracy, there remain outstanding challenges that need to be overcome, especially in shallow-water environments and in the extreme and high-latitude environments. The principal limitations of modern tide models in polar regions arise from a combination of poor bathymetry (especially seabed depth under the large Antarctic ice shelves) and relatively sparse and poor quality data for model validation and assimilation. The substantial lack of data in polar regions must be addressed. We suggest that more bottom pressure gauges should be deployed at specific locations showing enhanced intermodel differences. As an example, it would be useful to deploy bottom pressure instruments in Baffin Bay, especially in Nares Strait connecting Baffin Bay to the Arctic Ocean. New GPS records on floating Antarctic ice shelves in the Weddell Sea have recently been obtained [*King et al.*, 2011a, 2011b]; comparable records over the Ross Ice Shelf would be useful to resolve uncertainties around old gravimeter sites.

We expect that new satellite data will be invaluable additions for polar regions. ICESat laser altimeter data, although limited by its short time series, were useful in the southernmost Antarctic ice shelves [*Ray*, 2008; *Padman et al.*, 2008]. Existing and future CryoSat-2, HY-2A, Sentinel-3, and ICESat-2 data will lengthen the time series and should considerably strengthen tidal inversions. Planned wide-swath altimeter missions are expected to overfly some polar seas, which will be beneficial; in addition, the high spatial resolution of such altimetry will help resolve short-scale tides in all shallow seas. Notwithstanding these new data, satellites over polar regions are unlikely to be the panacea they have been in lower latitudes, for several reasons. (1) All high-inclination satellites have inferior tidal aliasing characteristics, with generally one or more constituents aliased to very long periods. (2) Sea ice can considerably complicate retrievals of sea levels, even for smaller-footprint altimeters. (3) Altimetry over floating ice shelves will remain less accurate than open-ocean altimetry owing to unavoidable changes in the ice and snow cover.

Since GRACE data appear to be one of the best tools for identifying high-latitude tide model errors (e.g., Figure 9), these data in principle supply valuable information for constraining models. Some early efforts at assimilating such data have begun [*Egbert et al.*, 2009], but the inherently coarse spatial resolution of satellite gravimetry requires that any assimilation must continue to give heavy weight to dynamical constraints to prevent corrupting shorter scales. Thus, the proper exploitation of GRACE data will necessitate continued reliance on hydrodynamic modeling, with its associated requirements for improved dynamics and improved bathymetric information.

The need for improved bathymetric data sets is a theme that runs through all types of tide modeling, whether in the open ocean, shelf areas, or high latitudes. It has long been known that bathymetry is especially important for shelf tide modeling, but the required accurate data sets are often lacking. The estimation of bathymetry from altimetry data works much less well in shelf regions than in the open ocean [*Smith and Sandwell*, 1997]. Thus, our knowledge of shelf bathymetry relies on acoustic soundings, which for many regions of the world are not in the public domain. In polar regions updated bathymetric bathymetry products are being developed, using a combination of traditional depth sounder and swath mapping along ship tracks combined with interpretation of gravity records from satellites and airborne surveys [*Jakobsson et al.*, 2012; *Arndt et al.*, 2013], and should be incorporated into global tide model grids. For specific regions of large tidal error, e.g., Larsen C Ice Shelf in the Weddell Sea, detailed surveys with airborne gravimetry

[*Cochran and Bell*, 2012] and seismic surveys [*Brisbourne et al.*, 2014] can deliver vastly improved water column thickness information. Coordinated international efforts to improve bathymetric data sets remain crucial for tide modeling.

For continued advances in shelf and polar regions we expect data assimilation into hydrodynamic models to play a larger and larger role. In light of that, it is encouraging to note the progress that has been achieved in the field of purely hydrodynamic, or forward, tide modeling. Such models have advanced in recent years as a result of more powerful computational capabilities, more accurate and higher-resolution bathymetric data, and better physics incorporating findings from analyses of altimeter data. One important lesson has been the need for a gravity wave drag mechanism in forward models. Improved unconstrained models thus reflect progress in understanding tidal dynamics. For the M_2 constituent, totally unconstrained global models are now about as accurate as the circa 1980 Schwiderski solution (see Figure 12). Notwithstanding these advancements, in terms of accuracy of tidal predictions, unconstrained models are not competitive with models that assimilate altimetry.

In addition to improved bathymetry, tidal hydrodynamic modeling is intertwined with questions concerning tidal energy dissipation and potential interactions with the oceanic general circulation. The various parameterizations of dissipation, the energy loss through interactions with sea ice and ice shelves, the exchange of energy between barotropic and baroclinic motion, and the physics of internal wave drag remain outstanding topics for investigation. Further, we need improved understanding and modeling strategies of the seasonal variations of barotropic tides induced by interactions between barotropic tides and stratification as well as seasonal ice coverage [e.g., *Ray et al.*, 2011; *Müller et al.*, 2014; *Fok et al.*, 2013].

Dynamically consistent data assimilation seems a key way forward [e.g., *Egbert*, 1997; *Taguchi et al.*, 2014], potentially allowing for simultaneous estimation of uncertain model parameters (e.g., bottom topography or dissipation) [cf., *Losch and Wunsch*, 2003]. Eventually, the validity of the current practice of separating tidal motions from the oceanic general circulation will start to break down, ultimately requiring ocean and climate models to have tides and their effects directly included. Two of the nonassimilative forward models we tested here are beginning steps in that direction.

The study of the tides began long ago as an essential part of nautical life [*Cartwright*, 1999]. The subject led to breakthroughs in basic geophysical science and also in accurate tidal predictions of extraordinary practical and scientific utility. We expect that future advances will continue to yield new insights into the nature of the ocean while continuing the long heritage of remarkably diverse applications.

Acknowledgments

We thank Phil Woodworth, Jean-Marie Beckers, and Carl Wunsch for comments on the original manuscript, and we thank Terry Williams, Bryant Loomis, and Andy Griffin for help with GRACE data processing. We acknowledge use of the Global Multi-Archive Current Meter Database, maintained by Robert Scott and Darran Furnival, in section 8.1. This work was funded in part through the German Science Foundation (DFG) SPP 1257 (projects DAROTA and DYNTIDE) and through the DFG-funded excellence initiative CLISAP. Authors F.G.G., S.B.L., and R.D.R. were supported by the U.S. National Aeronautics and Space Administration through the Ocean Surface Topography and GRACE programs. M.A.K. is a recipient of an Australian Research Council Future Fellowship (project FT110100207). J.A.M.G.'s work was done under a Natural Environmental Research Council Advanced Fellowship (NE/F014821/). B.K.A. acknowledges support from Office of Naval Research (ONR) grant N00014-11-1-0487. J.G.R. and J.F.S. were supported by the projects "Eddy resolving global ocean prediction including tides" and "Ageostrophic vorticity dynamics" sponsored by ONR under program element 0602435N. B.K.A., J.G.R., and J.F.S. acknowledge a grant for computer time from the Department of Defense High Performance Computing Modernization Program at the Navy DSRC. This is Naval Research Laboratory contribution NRL/JA/7320-14-2098 and has been approved for public release. S.D.G. and V.L. were supported through Natural Environment Research Council grant NE/I013563/1. The far-field component of the Hawaiian Ocean Mixing Experiment and the deployment of the associated acoustic tomography arrays were supported by grants OCE-9819527 and OCE98-19525 from the National Science Foundation. H.S.F. and Y.C. acknowledge support through the National Natural Science Foundation of China (grants 41374010 and 41306194). C.K.S., H.S.F., and Y.C.Y. were partially supported by NASA's Advanced Geodesy Program (grant NNX12AK28G) and by the Chinese Academy of Sciences/SAFEA International Partnership Program for Creative Research Teams (grant KZZD-EW-TZ-05).

The Editor on this paper was Eelco Rohling. He thanks Philip L. Woodworth and two anonymous reviewers for their review assistance on this manuscript.

References

Accad, Y., and C. L. Pekeris (1978), Solution of tidal equations for M_2 and S_2 tides in world oceans from a knowledge of tidal potential alone, *Philos. Trans. R. Soc., A290*, 235–266.

Andersen, O. B. (1995), Global ocean tides from ERS-1 and Topex/Poseidon altimeter, *J. Geophys. Res.*, *100*(C12), 25,249–25,259.

Andersen, O. B. (1999), Shallow water tides on the northwest European shelf from Topex/Poseidon altimeter, *J. Geophys. Res.*, *104*, 7729–7741.

Andersen, O. B., P. L. Woodworth, and R. A. Flather (1995), Intercomparison of recent ocean tide models, *J. Geophys. Res.*, *100*(C12), 25,261–25,282.

Antonov, J. I., D. Seidov, T. P. Boyer, R. A. Locarnini, A. V. Mishonov, H. E. Garcia, O. K. Baranova, M. M. Zweng, and D. R. Johnson (2010), *World Ocean Atlas 2009, Volume 2: Salinity,* edited by S. Levitus, 184 pp., NOAA Atlas NESDIS 69, U.S. Government Printing Office, Washington, D. C.

Arbic, B. K., S. T. Garner, R. W. Hallberg, and H. L. Simmons (2004), The accuracy of surface elevations in forward global barotropic and baroclinic tide models, *Deep Sea Res., Part II*, *51*, 3069–3101, doi:10.1016/j.dsr2.2004.09.014.

Arbic, B. K., J. X. Mitrovica, D. R. MacAyeal, and G. A. Milne (2008), On the factors behind large Labrador Sea tides during the last glacial cycle and the potential implications for Heinrich events, *Paleoceanography*, *23*, PA3211, doi:10.1029/2007PA001573.

Arbic, B. K., A. J. Wallcraft, and E. J. Metzger (2010), Concurrent simulation of the eddying general circulation and tides in a global ocean model, *Ocean Modell.*, *32*, 175–187, doi:10.1016/j.ocemod.2010.01.007.

Arbic, B. K, J. G. Richman, J. F. Shriver, P. G. Timko, E. J. Metzger, and A. J. Wallcraft (2012), Global modeling of internal tides within an eddying ocean general circulation model, *Oceanography*, *25*, 20–29, doi:10.5670/oceanog.2012.38.

Arndt, J. E., et al. (2013), The International Bathymetric Chart of the Southern Ocean (IBCSO) Version 1.0—A new bathymetric compilation covering circum-Antarctic waters, *Geophys. Res. Lett.*, *40*, 3111–3117, doi:10.1002/grl.50413.

Beardsley, R. C., T. F. Duda, J. F. Lynch, J. D. Irish, R. S. Ramp, C.-S. Chiu, T. Y. Tang, Y.-J. Yang, and G. Fang (2004), Barotropic tide in the northeast South China Sea, *IEEE J. Oceanic Eng.*, *29*, 1075–1086.

Becker, J. J., et al. (2009), Global bathymetry and elevation data at 30 arc seconds resolution: SRTM30_PLUS, *Mar. Geod.*, *32*(4), 355–371.

Bernard, E. N., C. Meinig, V. V. Titov, K. O'Neil, R. Lawson, K. Jarrott, R. Bailey, F. Nelson, S. Tinti, C. von Hillebrandt, and P. Koltermann (2010), Tsunami resilient communities, in *Proceedings of the OceanObs09: Sustained Ocean Observations and Information for Society Conference*, vol. 1, edited by J. Hall, D. E. Harrison, and D. Stammer, p. 4, ESA Publication WPP-306, Venice, Italy.

Book, J. W., H. Perkins, and M. Wimbush (2009), North Adriatic tides: Observations, variational data assimilation modeling, and linear tide dynamics, *Geofizika*, *26*, 115–143.

Bosch, W., R. Savcenko, F. Flechtner, C. Dahle, T. Mayer-Gürt, D. Stammer, E. Taguchi, and K.-H. Ilk (2009), Residual ocean tides signals from satellite altimetry, GRACE gravity fields, and hydrodynamic modeling, *Geophys. J. Int.*, *178*, 1185–1192, doi:10.1111/j.1365-246X.2009.04281.x.

Brisbourne, A. M., A. M. Smith, E. C. King, K. W. Nicholls, P. R. Holland, and K. Makinson (2014), Seabed topography beneath Larsen C Ice Shelf from seismic soundings, *The Cryosphere*, *8*, 1–13, doi:10.5194/tc-8-1-2014.

Carrère, L., and F. Lyard (2003), Modeling the barotropic response of the global ocean to atmospheric wind and pressure forcing: Comparisons with observations, *Geophys. Res. Lett.*, *30*(6), 1275, doi:10.1029/2002GL016473.

Carrère, L., F. Lyard, M. Cancet, A. Guillot, and L. Roblou (2012), FES 2012: A new global tidal model taking advantage of nearly 20 years of altimetry, paper presented at The Symposium 20 Years of Progress in Radar Altimetry, Venice.

Cartwright, D. E. (1999), *Tides: A Scientific History*, Cambridge Univ. Press, New York.

Cartwright, D. E., and R. D. Ray (1990), Oceanic tides from Geosat altimetry, *J. Geophys. Res.*, *95*, 3069–3090.

Cartwright, D. E., and R. D. Ray (1991), Energetics of global ocean tides from Geosat altimetry, *J. Geophys. Res.*, *96*, 16897–16912.

Chassignet, E. P., H. E. Hurlburt, O. M. Smedstad, G. R. Halliwell, P. J. Hogan, A. J. Wallcraft, R. Baraille, and R. Bleck (2007), The HYCOM (HYbrid Coordinate Ocean Model) data assimilative system, *J. Mar. Syst.*, *65*, 60–83, doi:10.1016/j.marsys.20-05.09.016.

Cheng, Y., and O. B. Andersen (2011), Multimission empirical ocean tide modeling for shallow waters and polar seas, *J. Geophys. Res.*, *116*, C11001, doi:10.1029/2011JC007172.

Cochran, J., and R. Bell (2012), Inversion of IceBridge gravity data for continental shelf bathymetry beneath the Larsen Ice Shelf, *J. Glaciol.*, *58*, 540–552.

Dushaw, B. D., P. F. Worcester, and B. D. Cornuelle (1994), Barotropic currents and vorticity in the central North Pacific Ocean during summer 1987 determined from long-range reciprocal acoustic transmissions, *J. Geophys. Res.*, *99*, 3263–3272.

Dushaw, B. D., B. D. Cornuelle, P. Worcester, B. M. Howe, and D. S. Luther (1995), Barotropic and baroclinic tides in the central North Pacific Ocean determined from long-range reciprocal acoustic transmissions, *J. Phys. Oceanogr.*, *25*, 631–647.

Dushaw, B. D., G. D. Egbert, P. Worcester, B. Cornuelle, B. Howe, and K. Metzger (1997), A Topex/POSIEDON global tidal model (TPXO.2) and barotropic tidal currents determined from long-range acoustic transmissions, *Prog. Oceanogr.*, *40*, 337–367.

Dushaw, B. D., P. F. Worcester, and M. A. Dzieciuch (2011), On the predictability of mode-1 internal tides, *Deep Sea Res., Part I*, *58*, 677–698, doi:10.1016/j.dsr.2011.04.002.

Eanes, R., and S. Bettadpur (1996), The CSR 3.0 global ocean tide model, *Tech. Memo. CSR-TM-96-05*, Center for Space Res., Univ. Texas, Austin.

Egbert, G. D. (1997), Tidal data inversion: Interpolation and inference, *Prog. Oceanogr.*, *40*, 53–80.

Egbert, G. D., and A. F. Bennett (1996), Data assimilation methods for ocean tides, in *Modern Approaches to Data Assimilation in Ocean Modeling*, edited by P. Malanotte-Rizzoli, pp. 147–179, Elsevier, Amsterdam, The Netherlands.

Egbert, G. D., and S. Y. Erofeeva (2002), Efficient inverse modeling of barotropic ocean tides, *J. Atmos. Oceanic Tech.*, *19*, 183–204.

Egbert, G. D., and R. D. Ray (2000), Significant dissipation of tidal energy in the deep ocean inferred from satellite altimeter data, *Nature*, *405*, 775–778.

Egbert, G. D., and R. D. Ray (2001), Estimates of M_2 tidal energy dissipation from Topex/Poseidon altimeter data, *J. Geophys. Res.*, *106*, 22475–22502.

Egbert, G. D., A. F. Bennett, and M. G. G. Foreman (1994), Topex/Poseidon tides estimated using a global inverse model, *J. Geophys. Res.*, *99*, 24821–24852.

Egbert, G. D., R. D. Ray, and B. G. Bills (2004), Numerical modeling of the global semidiurnal tide in the present day and in the last glacial maximum, *J. Geophys. Res.*, *109*, C03003, doi:10.1029/2003JC001973.

Egbert, G. D., S. Y. Erofeeva, S. C. Han, S. B. Luthcke, and R. D. Ray (2009), Assimilation of GRACE tide solutions into a numerical hydrodynamic inverse model, *Geophys. Res. Lett.*, *36*, L20609, doi:10.1029/2009GL040376.

Egbert, G. D., S. Y. Erofeeva, and R. D. Ray (2010), Assimilation of altimetry data for nonlinear shallow-water tides: Quarter-diurnal tides of the Northwest European Shelf, *Cont. Shelf Res.*, *30*, 668–679.

Ferry, N., et al. (2012), *GLORYS2V1 Global Ocean Reanalysis of the Altimetric Era (1992–2009) at Meso Scale*, Mercator Quarterly Newsletter 44, Mercator Océan, Ramonville Saint-Agne, France. [Available at http://www.mercator-ocean.fr/eng/actualites-agenda/newsletter/newsletter-Newsletter-44-Various-areas-of-benefit-using-the-Mercator-Ocean-products.]

Fok, H. S. (2012), Ocean tides modeling using satellite altimetry, *Geodetic Science Rep. No. 501*, Ohio State Univ., Columbus.

Fok, H. S., C. K. Shum, Y. Yi, A. Braun, and H. Baki Iz (2013), Evidences of seasonal variation in altimetry derived ocean tides in the Subarctic Ocean, *Terr. Atmos. Ocean. Sci.*, *24*(4), 605–613, doi:10.3319/TAO.2012.11.16.01(TibXS).

Fu, L.-L., and A. Cazenave (Eds.) (2001), *Satellite Altimetry and Earth Sciences: A Handbook of Techniques and Applications*, 463 pp., Academic Press, San Diego, Calif.

GEBCO Digital Atlas (2003), *British Oceanographic Data Centre on Behalf of IOC, IHO and BODC*, Centenary Edition of the GEBCO Digital Atlas, published on CD-ROM on behalf of the Intergovernmental Oceanographic Commission and the International Hydrographic Organization as part of the General Bathymetric Chart of the Oceans, British Oceanographic Data Centre, Liverpool, U. K.

Gill, A. E. (1982), *Atmosphere-Ocean Dynamics*, 662 pp., Academic Press, San Diego, Calif.

Green, J. A. M., and J. Nycander (2013), A comparison of internal wave-drag parameterizations for tidal models, *J. Phys. Oceanogr.*, *43*, 104–119.

Griffiths, S. D. (2013), Kelvin wave propagation along straight boundaries in C-grid finite-difference models, *J. Comput. Phys.*, *255*, 639–659, doi:10.1016/j.jcp.2013.08.040.

Griffiths, S. D., and W. R. Peltier (2009), Modeling of polar ocean tides at the last glacial maximum: Amplification, sensitivity, and climatological implications, *J. Clim.*, *22*, 2905–2924, doi:10.1175/2008JCLI2540.1.

Groves, G. W., and R. W. Reynolds (1975), An orthogonalized convolution method of tide prediction, *J. Geophys. Res.*, *80*, 4131–4138.

Hallberg, R. W., and P. B. Rhines (1996), Buoyancy-driven circulation in an ocean basin with isopycnals intersecting the sloping boundary, *J. Phys. Oceanogr.*, *26*, 913–940.

Han, S.-C., R. D. Ray, and S. B. Luthcke (2007), Ocean tidal solutions in Antarctica from GRACE inter-satellite tracking data, *Geophys. Res. Lett.*, *34*, L21607, doi:10.1029/2007GL031540.

Hendershott, M. C. (1972), The effects of solid earth deformation on global ocean tides, *Geophys. J. Astron. Soc.*, *29*, 389–402.

Hill, D. F., S. D. Griffiths, W. R. Peltier, B. P. Horton, and T. E. Tornqvist (2011), High-resolution numerical modeling of tides in the western Atlantic, Gulf of Mexico, and Caribbean Sea during the Holocene, *J. Geophys. Res.*, *116*, C10014, doi:10.1029/2010JC006896.

Jakobsson, M., et al. (2012), The International Bathymetric Chart of the Arctic Ocean (IBCAO) Version 3.0, *Geophys. Res. Lett.*, *39*, L12609, doi:10.1029/2012GL052219.

Jayne, S. R., and L. C. St. Laurent (2001), Parameterizing tidal dissipation over rough topography, *Geophys. Res. Lett.*, *28*, 811–814, doi:10.1029/2000GL012044.
Killett, B., J. Wahr, S. D. Desai, D. Yuan, and M. Watkins (2011), Arctic Ocean tides from GRACE accelerations, *J. Geophys. Res.*, *116*, C11005, doi:10.1029/2011JC007111.
Kim, T.-H., K. Shibuyaa, K. Doia, Y. Aoyamaa, and H. Hayakawab (2011), Validation of global ocean tide models using the superconducting gravimeter data at Syowa Station, Antarctica, and in situ tide gauge and bottom-pressure observations, *Polar Science*, *5*, 21–39.
King, M. A., L. Padman, K. Nicholls, P. J. Clarke, G. H. Gudmundsson, B. Kulessa, and A. Shepherd (2011a), Ocean tides in the Weddell Sea: New observations on the Filchner-Ronne and Larsen C ice shelves and model validation, *J. Geophys. Res.*, *116*, C06006, doi:10.1029/2011JC006949.
King, M. A., L. Padman, K. Nicholls, P. J. Clarke, G. H. Gudmundsson, B. Kulessa, A. Shepherd, and N. Gourmelen (2011b), Correction to "Ocean tides in the Weddell Sea: New observations on the Filchner-Ronne and Larsen C ice shelves and model validation", *J. Geophys. Res.*, *116*, C08026, doi:10.1029/2011JC007463.
King, M. A., and L. Padman (2005), Accuracy assessment of ocean tide models around Antarctica, *Geophys. Res. Lett.*, *32*, L23608, doi:10.1029/2005GL023901.
Koop, R., and R. Rummel (Eds.) (2008), *The Future of Satellite Gravimetry*, ESTEC, Noordwijk, The Netherlands.
Kowalik, Z., and A. Y. Proshutinsky (1994), The Arctic Ocean tides, in *The Polar Oceans and Their Role in Shaping the Global Environment, Geophys. Monogr. Ser.*, vol. 85, edited by O. M. Johannessen, R. D. Muench, and J. E. Overland, pp. 137–158, AGU, Washington, D. C.
Lambeck, K. (1988), *Geophysical Geodesy*, Clarendon Press, Oxford, U. K.
Le Provost, C., M. L. Genco, F. Lyard, P. Vincent, and P. Canceil (1994), Tidal spectroscopy of the world ocean tides from a finite element hydrodynamic model, *J. Geophys. Res.*, *99*(C12), 24,777–24,798.
Liu, W. T., and X. Xie (2006), Measuring ocean surface wind from space, in *Remote Sensing of the Marine Environment: Manual of Remote Sensing*, vol. 6, 3rd ed., edited by J. Gower, pp. 149–178, Am. Soc. for Photogram. and Remote Sensing, Bethesda, Md.
Locarnini, R. A., A. V. Mishonov, J. I. Antonov, T. P. Boyer, H. E. Garcia, O. K. Baranova, M. M. Zweng, and D. R. Johnson (2010), *World Ocean Atlas 2009, Volume 1: Temperature,* edited by S. Levitus, 184 pp., NOAA Atlas NESDIS 68, U.S. Government Printing Office, Washington, D. C.
Losch, M., and C. Wunsch (2003), Bottom topography as a control variable in an ocean model, *J. Atmos. Oceanic Technol.*, *20*, 1685–1696.
Luthcke, S. B., D. D. Rowlands, F. G. Lemoine, S. M. Klosko, D. Chinn, and J. J. McCarthy (2006), Monthly spherical harmonic gravity field solutions determined from GRACE inter-satellite range-rate data alone, *Geophys. Res. Lett.*, *33*, L02402, doi:10.1029/2005GL024846.
Luther, D. S., J. H. Filloux, and A. D. Chave (1991), Low-frequency, motionally induced electromagnetic fields in the ocean 2: Electric field and Eulerian current comparison, *J. Geophys. Res.*, *96*, 12797–12814.
Luyten, J. R., and H. M. Stommel (1991), Comparison of M_2 tidal currents observed by some deep moored current meters with those of the Schwiderski and Laplace models, *Deep Sea Res. Part A*, *38*, S573–S589.
Lyard, F., F. Lefevre, T. Letellier, and O. Francis (2006), Modelling the global ocean tides: Modern insights from FES2004, *Ocean Dyn.*, *56*, 394–415.
Marsland, S., H. Haak, J. H. Jungclaus, M. Latif, and F. Röske (2003), The Max-Planck-Institute global ocean/sea ice model with orthogonal curvilinear coordinates, *Ocean Modell.*, *5*, 91–127.
Matsumoto, K., T. Takanezawa, and M. Ooe (2000), Ocean tide models developed by assimilating Topex/Poseidon altimeter data into hydro- dynamical model: A global model and a regional model around Japan, *J. Oceanogr.*, *56*, 567–581.
Metzger, E. J., O. M. Smedstad, P. G. Thoppil, H. E. Hurlburt, D. S. Franklin, G. Peggion, J. F. Shriver, and A. J. Wallcraft (2010), Validation test report for the global ocean forecast system V3.0–1/12° HYCOM/NCODA: Phase II, *NRL Memo. Report, NRL/MR/7320–10-9236*, Naval Research Laboratory, Oceanography Division, Stennis Space Center.
Miller, A. J., D. S. Luther, and M. C. Hendershott (1993), The fortnightly and monthly tides—Resonant Rossby waves or nearly equilibrium gravity-waves, *J. Phys. Oceanogr.*, *23*, 879–897.
Müller, M. (2013), On the space- and time-dependence of barotropic-to-baroclinic tidal energy conversion, *Ocean Modell.*, *72*, 242–252, doi:10.1016/j.ocemod.2013.09.00.
Müller, M., J. Y. Cherniawsky, M. G. G. Foreman, and J.-S. von Storch (2012), Global map of M_2 internal tide and its seasonal variability from high resolution ocean circulation and tide modeling, *Geophys. Res. Lett.*, *39*, L19607, doi:10.1029/2012GL053320.
Müller, M., J. Cherniawsky, M. Foreman, and J.-S. von Storch (2014), Seasonal variation of the $M_2$2 tide, *Ocean Dyn.*, *64*(2), 159–177, doi:10.1007/s10236-013-0679-0.
Munk, W. (1997), Once again: Once again—Tidal friction, *Progr. Oceanogr.*, *40*, 7–35.
Nycander, J. (2005), Generation of internal waves in the deep ocean by tides, *J. Geophys. Res.*, *110*, C10028, doi:10.1029/2004JC002487.
Oreiro, F. A., E. D'Onofrioa, W. Grismeyera, M. Fiorea, and M. Saracenoc (2014), Comparison of tide model outputs for the northern region of the Antarctic Peninsula using satellite altimeters and tide gauge data, *Polar Sci.*, *8*, 10–23, doi:10.1016/j.polar.2013.12.001.
Padman, L., S. Y. Erofeeva, and H. A. Fricker (2008), Improving Antarctic tide models by assimilation of ICESat laser altimetry over ice shelves, *Geophys. Res. Lett.*, *35*, L22504, doi:10.1029/2008GL035592.
Parke, M. E., and M. C. Hendershott (1980), M2, S2, K1 models of the global ocean tide on an elastic earth, *Mar. Geod.*, *3*, 379–408.
Pekeris, C. L., and Y. Accad (1969), Solution of Laplace's equations for the M_2 tide in the world oceans, *Philos. Trans. R. Soc. A*, *A265*, 413–436.
Ponchaut, F., F. Lyard, and C. Le Provost (2001), An analysis of the tidal signal in the WOCE sea level dataset, *J. Atmos. Oceanic Technol.*, *18*, 77–91, doi:10.1175/1520-0426(2001)018<0077:AAOTTS>2.0.CO;2.
Pugh, D. T. (1987), *Tides, Surges and Mean Sea-Level: A Handbook for Scientists and Engineers*, 472 pp., John Wiley, Chichester, U. K.
Pugh, D. T., and P. L. Woodworth (2014), *Sea-Level Science: Understanding Tides, Surges Tsunamis and Mean Sea-Level Changes*, 407 pp., Cambridge Univ. Press, Cambridge, U. K.
Ray, R. D. (1999), A global ocean tide model from Topex/Poseidon altimetry: GOT99.2, *NASA Tech. Memo. 209478*, 58 pp., Goddard Space Flight Center, Greenbelt, MD.
Ray, R. D. (2001), Inversion of oceanic tidal currents from measured elevations, *J. Mar. Syst.*, *28*, 1–18.
Ray, R. D. (2008), A preliminary tidal analysis of ICESat laser altimetry: Southern Ross Ice Shelf, *Geophys. Res. Lett.*, *35*, L02505, doi:10.1029/2007GL032125.
Ray, R. D. (2013), Precise comparisons of bottom-pressure and altimetric ocean tides, *J. Geophys. Res. Oceans*, *118*, 4570–4584, doi:10.1002/jgrc.20336.
Ray, R. D., and G. D. Egbert (1997), The flux of tidal energy across latitude 60°S, *Geophys. Res. Lett.*, *24*, 543–546.
Ray, R. D., S. B. Luthcke, and J.-P. Boy (2009), Qualitative comparisons of global ocean tide models by analysis of intersatellite ranging data, *J. Geophys. Res.*, *114*, C09017, doi:10.1029/2009JC005362.

Ray, R. D., G. D. Egbert, and S. Y. Erofeeva (2011), Tide predictions in shelf and coastal waters: Status and prospects, in *Coastal Altimetry*, edited by S. Vignudelli et al., pp. 191–216, Springer-Verlag, Berlin, Germany.

Richter, A., L. Mendoza, R. Perdomo, J. Hormaechea, R. Savcenko, W. Bosch, and R. Dietrich (2012), Pressure tide gauge records from the Atlantic shelf off Tierra del Fuego, southernmost South America, *Cont. Shelf Res.*, *42*, 20–29.

Rosmond, T. E., J. Teixeira, M. Peng, T. F. Hogan, and R. Pauley (2002), Navy Operational Global Atmospheric Prediction System (NOGAPS): Forcing for ocean models, *Oceanography*, *15*, 99–108.

Rowlands, D. D., S. B. Luthcke, S. M. Klosko, F. G. R. Lemoine, D. S. Chinn, J. J. McCarthy, C. M. Cox, and O. B. Anderson (2005), Resolving mass flux at high spatial and temporal resolution using GRACE intersatellite measurements, *Geophys. Res. Lett.*, *32*(4), L04310, doi:10.1029/2004GL021908.

Rudnick, D. L., et al. (2003), From tides to mixing along the Hawaiian ridge, *Science*, *301*, 355–357.

Sammari, C., V. G. Koutitonsky, and M. Moussa (2006), Sea level variability and tidal resonance in the Gulf of Gabes, Tunisia, *Cont. Shelf Res.*, *26*, 338–350.

Savcenko, R., and W. Bosch (2012), EOT11a—Empirical ocean tide model from multi-mission satellite altimetry, *DGFI Report No. 89*, Deutsches Geodätisches Forschungsinstitut, München.

Scharroo, R. (2008), *RADS Version 3.1 User Manual and Format Specification*, 51 pp., Delft Univ. of Technology, The Netherlands.

Schrama, E. J. O., and R. D. Ray (1994), A preliminary tidal analysis of Topex/Poseidon altimetry, *J. Geophys. Res.*, *99*, 24,799–24,808.

Schwiderski, E. W. (1979), Global ocean tides: Part II. The semidiurnal principal lunar tide 884 (M_2). Atlas of Tidal Charts and Maps, *NSWC Tech. Rep. 79-414*, 87 pp., Naval Surface Weapons Center, Dahlgren, Va.

Scott, R. B., B. K. Arbic, E. P. Chassignet, A. C. Coward, M. Maltrud, W. J. Merryfield, A. Srinivasan, and A. Varghese (2010), Total kinetic energy in four global eddying ocean circulation models and over 5000 current meter records, *Ocean Modell.*, *32*, 157–169, doi:10.1016/j.ocemod.2010.01.005.

Seeber, G. (2003), *Satellite Geodesy*, 2nd ed., 589 pp., Walter de Gruyter, Berlin, Germany.

Shriver, J. F., B. K. Arbic, J. G. Richman, R. D. Ray, E. J. Metzger, A. J. Wallcraft, and P. G. Timko (2012), An evaluation of the barotropic and internal tides in a high resolution global ocean circulation model, *J. Geophys. Res.*, *117*, C10024, doi:10.1029/2012JC008170.

Shum, C. K., et al. (1997), Accuracy assessment of recent ocean tide models, *J. Geophys. Res.*, *102*, 25,173–25,194.

Smith, W. H. F., and D. T. Sandwell (1997), Global sea floor topography from satellite altimetry and ship depth soundings, *Science*, *277*, 1956–1962.

Taguchi, E., W. Zahel, and D. Stammer (2014), Inferring deep ocean tidal energy dissipation from the global high-resolution data-assimilative HAMTIDE model, *J. Geophys. Res. Oceans*, doi:10.1002/2013JC009766.

Tapley, B. D., S. Bettadpur, M. Watkins, and C. Reigber (2004), The gravity recovery and climate experiment: Mission overview and early results, *Geophys. Res. Lett.*, *31*, L09607, doi:10.1029/2004GL019920.

Teague, W. J., H. T. Perkins, Z. R. Hallock, and G. A. Jacobs (1998), Current and tide observations in the southern Yellow Sea, *J. Geophys. Res.*, *103*, 27,783–27,793.

Timko, P. G., B. K. Arbic, J. G. Richman, R. B. Scott, E. J. Metzger, and A. J. Wallcraft (2012), Skill tests of three-dimensional tidal currents in a global ocean model: A look at the North Atlantic, *J. Geophys. Res.*, *117*, C08014, doi:10.1029/2011JC007617.

Timko, P. G., B. K. Arbic, J. G. Richman, R. B. Scott, E. J. Metzger, and A. J. Wallcraft (2013), Skill testing a three-dimensional global tide model to historical current meter records, *J. Geophys. Res. Oceans*, *118*, 6914–6933, doi:10.1002/2013JC009071.

von Storch, J.-S., C. Eden, I. Fast, H. Haak, D. Hernández-Deckers, E. Maier-Reimer, J. Marotzke, and D. Stammer (2012), An estimate of Lorenz energy cycle for the world ocean based on the STORM/NCEP simulation, *J. Phys. Oceanogr.*, *42*, 2185–2205.

Vignudelli, S., A. G. Kostianoy, P. Cipollini, and J. Benveniste (2011), *Coastal Altimetry*, Springer-Verlag, Berlin, Germany.

Visser, P. N. A. M., N. Sneeuw, T. Reubelt, M. Losch, and T. van Dam (2010), Space-borne gravimetric satellite constellation and ocean tides: Aliasing effects, *Geophys. J. Int.*, *181*, 789–805.

Vlasenko, V., N. Stashchuk, and K. Hutter (2005), *Baroclinic Tides: Theoretical Modeling and Observational Evidence*, 351 pp., Cambridge Univ. Press, Cambridge, U. K.

Wiese, D. N. (2011), Optimizing two pairs of GRACE-like satellites for recovering temporal gravity variations, PhD thesis, Univ. of Colorado, Boulder, Colo.

Wiese, D. N., P. Visser, and R. S. Nerem (2011), Estimating low resolution gravity fields at short time intervals to reduce temporal aliasing errors, *Adv. Space Res.*, *48*, 1094–1107.

Wilhelm, H., W. Zürn, and H.-G. Wenzel (1997), *Tidal Phenomena*, Springer, Berlin, Germany.

Williamson, R. G., and J. G. Marsh (1985), Starlette geodynamics: The Earth's tidal response, *J. Geophys. Res.*, *90*, 9346–9352.

Wunsch, C. (1967), The long-period tides, *Rev. Geophys.*, *5*, 447–476.

Wunsch, C. (1975), Internal tides in the ocean, *Rev. Geophys.*, *13*, 167–182.

Yao, Z., R. He, X. Bao, D. Wu, and J. Song (2012), M_2 tidal dynamics in the Bohai and Yellow Seas: A hybrid data assimilative modeling study, *Ocean Dyn.*, *62*, 753–769.

Zahel, W. (1995), Assimilating ocean tide determined data into global tidal models, *J. Mar. Syst.*, *6*, 3–13.